

NEW FRONTIERS IN CHEMISTRY

New Front. Chem.

(former Annals of West University of Timișoara – Series of Chemistry)

(2018) Volume 27, Number (Issue) 2, pp. 51-113

Ordinary Issue

TABLE OF CONTENTS

Sol Gel Derived Silica Matrix. Solution Concentration of the Supplied Catalyst Influence upon Nanoporous Material Morpho-Textural Properties	51-65
Mirela Piciorus, Ana-Maria Putz, Nicola Roxana, Adelina Andelescu, Catalin Ianasi, Paula Sfirloaga, and Cecilia Savii	
The effects of ions in amniotic fluid in development of fetus	67-71
Radu Neamtu, Ion Neamtu, Andrei Motoc	
Electrochemical Systems and Mechanically Interlocked Molecules. Part 1: Nano-Science	73-87
Mirela I. Iorga, Marius C. Mirica, and Mihai V. Putz	
Electrochemical Systems and Mechanically Interlocked Molecules. Part 1: Nano-Technology	89-104
Mirela I. Iorga, Paula Svera, Doru Buzatu, and Mihai V. Putz	
Topological evolution of the 5 8 5 defect in graphene	105-113
Ottorino Ori and Mihai V. Putz	

PUBLISHER:
 **Universitatea de Vest**
din Timișoara

NEW FRONTIERS IN CHEMISTRY: METADATA

New Frontiers in Chemistry (New Front. Chem.) is an open-access fee-free peer-review international academic journal addressing the modern trends and frontiers in fundamental, applicative and multidisciplinary chemistry, paralleling the ever-expanding chemical data, methods, and compounds available and continuously produced, towards cross fertilizing the multidisciplinary ideas as coming from Chemistry combined with Mathematics, the Natural and Applied sciences (Physics, Biology, Medicine, Agriculture, Environmental, Engineering), and beyond.

NEW FRONTIERS IN CHEMISTRY
(NEW FRONT. CHEM.)
is published biannually by

West University of Timișoara
Blvd. V. Parvan 4
Timisoara 300223, ROMANIA
E-mail: newfrontchem@iqstorm.ro
Web: www.newfrontchem.iqstorm.ro

ISSN 2393 – 2171
ISSN-L 2393 – 2171

Subscription Price per Volume

Electronic: open access Print: on demand by above email address

Additional color graphics is available in the e-version of this Journal

Copyright © 2015 West University of Timișoara. Printed in Romania. Submission to publication implies authors have the right to assign the copyright for publication herein contained, and no right protected by copyright to their works have been previously assigned; Acceptation for publication implies that authors' works contain no matter that is libelous or is otherwise unlawful or that invades individual privacy or infringes any proprietary right or any statutory copyright; Publication implies the material is original (at least 50% updated or syntheses of previously published – appropriately cited – works are considered original); authors agree to indemnify and hold the Publisher harmless against any claim or judgment to the contrary; authors (and all coauthors) have the right to present orally in any forum all or part of their works. The Publisher, as copyright owner upon (e-)publication has authority to grant permission to reproduce the papers. The Publisher assumes no responsibility for any statements or fact or opinion expressed in the published papers.

NEW FRONTIERS IN CHEMISTRY: EDITORS

Editor-in-Chief:
(and Editorial Office of New Front. Chem.)

MIHAI V. PUTZ

West University of Timișoara (WUT)
Faculty of Chemistry, Biology, Geography (CBG)
Biology-Chemistry Department
Laboratory of Computational and Structural Physical-Chemistry for
Nanosciences and QSAR
Pestalozzi Street No.16, Timișoara, RO-300115
ROMANIA
Phone: +40-256-592638, Fax: +40-256-592620
Ems: mihai.putz@e-uvv.ro, mv_putz@yahoo.com

Senior Editor:

VASILE OSTAFE

West University of Timișoara
Faculty of Chemistry, Biology, Geography
Biology-Chemistry Department
Timișoara, ROMANIA
Ems: vasile.ostafe@e-uvv.ro, vostafe@yahoo.com

Assistant and Deputy Editor:

DANIELA DASCĂLU

West University of Timișoara
Faculty of Chemistry, Biology, Geography
Biology-Chemistry Department
Timișoara, ROMANIA
Em: dana_denisa_2005@yahoo.com

Editorial Board:

OTTORINO ORI

Actinium Chemical Research
Head of Nanochemistry Division
Rome, ITALY

ALINA ZAMFIR

University of Arad
Department of Chemistry and Biology
Arad, ROMANIA

MIRCEA V. DIUDEA

“Babes-Bolyai” University of Cluj-Napoca
Faculty of Chemistry and Chemical Engineering
Department of Organic Chemistry
Cluj-Napoca, ROMANIA

JOEL F. LIEBMAN

University of Maryland, Baltimore County (UMBC)
The Department of Chemistry and Biochemistry
Baltimore (MD), USA

FRANCESC MAS

University of Barcelona
Departament de Química Física
SPAIN

LIONELLO POGLIANI

Universitat de València
Facultat de Farmàcia
Unitat d'Investigació en Disseny de Farmacs i Connectivitat Molecular
SPAIN

MARILENA FERBINTEANU

University of Bucharest
Faculty of Chemistry
Inorganic Chemistry Department
ROMANIA

SPERANTA AVRAM

University of Bucharest
Faculty of Biology
Department of Anatomy, Animal Physiology and Biophysics
ROMANIA

FRANCO CATALDO

Actinium Chemical Research
General Director
Rome, ITALY

EUGENIA FAGADAR-COSMA

Institute of Chemistry Timisoara of Romanian Academy
Timisoara, ROMANIA

FRANCISCO TORRENS

Universitat de València
Institut Universitari de Ciència Molecular
SPAIN

NAZMUL ISLAM

Techno Global-Balurghat
Conceptual and General Chemistry
INDIA

MARGHERITA VENTURI

University of Bologna
Dipartimento di Chimica «Ciamician»
Bologna, ITALY

IONEL MANGALAGIU

University Alexandru Ioan Cuza of Iasi
Organic Chemistry Department
Iasi, ROMANIA

RADIVOJE PRODANOVIC

University of Belgrade
Department of Biochemistry
SERBIA

KATHLEEN SWALLOW

Emeritus at Merrimack College
Department Analytical Chemistry
USA

LÁSZLÓ ALMÁSY

Hungarian Academy of Sciences
Wigner Research Centre for Physics
Budapest, HUNGARY

Advisory Editors

(from members of Biology-Chemistry Department of West University of Timișoara):

VASILE OSTAFE (Biochemistry, Chromatography, Environmental Chemistry)
IONEL CIUCANU (Instrumental Techniques for Analytical Chemistry)
ADRIANA ISVORAN (Biophysics, Bioinformatics)
MIHAI V. PUTZ (Nanochemistry, Quantum Chemistry)
TITUS VLASE (Thermal Analysis, Chemical Kinetics, Chemistry of Solid State)
GABRIELA VLASE (Inorganic Chemistry, Thermal Analysis)
OTILIA BIZEREA (Inorganic Chemistry)
GABRIELA PREDA (Organic Chemistry, Catalysis)
CONSTANTIN BOLCU (Organic Chemistry, Polymers)
VLAD CHIRIAC (General and Analytical Chemistry, Electrochemistry)
DANA VLASCICI (Analytical Chemistry)
DANIELA DASCALU (Thermodynamics and Chemical Statistics)
CORINA DUDA-SEIMAN (QSAR, Organic Chemistry, Medicinal Chemistry)
LAURA PITULICE (Environmental Chemistry)
HORIA POPOVICI (Colloidal Chemistry, Analytical Chemistry)
BEATRICE VLAD-OROS (Chemical and Enzyme Kinetics)
MARIANA ALBULESCU (Organic Chemistry, Natural Compounds)
DORINA MODRA (Organic Chemistry)
MIRCEA SELEGEAN (Biotechnologies)
NICOLETA IANOVIC (Aerobiology, Plant Physiology)

Honorary Editors

(as Doctor Honoris Causa of WUT/CBG & Formers Editors and Developers of Annals of West University of Timișoara - Series Chem.):

ALEXANDRU BALABAN (Texas A&M University at Galveston, USA, & Romanian Academy, Romania)
HAGEN KLEINERT (Berlin Free University, Germany)
KATLEEN SWALLOW (Merrimack College, USA)
GABOR NÁRÁY-SZABÓ ("Lorand Eötvös" University Budapest, Hungary)
EUGEN SEGAL (University of Bucharest, Romanian Academy, Romania)
VICTOR EMANUEL SAHINI (Polytechnic Bucharest, Romanian Academy, Romania)
MARIUS ANDRUH (Romanian Academy, Bucharest)
ZENO SIMON (Romanian Academy, Romania)
ADRIAN CHIRIAC (West University of Timisoara, Romania)
MIRCEA MRACEC (West University of Timisoara, Romania)
VASILE OSTAFE (West University of Timisoara, Romania)
NICOLAE BONCIOCAT (†, Babes-Bolyai University, Cluj-Napoca, Romania)
ALAN R. KATRITZKY (†, University of Florida, Gainesville, USA)

Article

Sol Gel Derived Silica Matrix. Solution Concentration of the Supplied Catalyst Influence upon Nanoporous Material Morpho-Textural Properties

MIRELA PICIORUS¹, ANA-MARIA PUTZ¹, NICOLA ROXANA¹,
ADELINA ANDELESCU¹, CATALIN IANASI¹, PAULA SFIRLOAGA²,
AND CECILIA SAVII¹

1) Institute of Chemistry Timisoara of the Romanian Academy, 24 Mihai Viteazul Bdl., 300223, Timisoara, Romania

2) National Institute for Research and Development in Electrochemistry and Condensed Matter, 144 Prof. Dr. Aurel Paunescu Podeanu Str., Timisoara, Romania

ABSTRACT

Template free, base catalysed sol-gel route (Stöber method) and low power sonic-activated sol-gel process (20 kHz ultrasonic bath) were used to obtain two series of samples. The influence of the concentration of the supplying ammonia solution upon the silica sols stability and solid products properties was followed. The reactants molar ratio TEOS: H₂O: ETOH: NH₃ of 1: 25: 20: 0.2 was rigorously kept constant. We have examined the influence of adding the ammonia solutions of different concentrations, specifically: 25% NH₃, 12% NH₃, 6% NH₃, and 3% NH₃. Either relatively stable colloidal suspensions or precipitates were obtained. The silica sols stability was related to the evolution of the turbidity over time. The resulted solid materials, xerogel's and sonogel's texture and morphology have been studied by using BET, SEM techniques. FT-IR was used to exhibit the main silica bonds. It was observed that by supplying base catalyst of variable concentrations, by changing initial pH of the process, it makes a difference concerning silica suspension behaviour and also in silica particle morphology. The used variable produced distinct effects upon both classic process and resulted xerogels, and sonoactivated sol-gel process and resulted sonogels. For all concentrations of ammonia solution, by classic sol-gel process, silica precipitates were obtained, and under ultrasonic field action, relatively stable translucent silica colloids resulted.

Keywords: sol-gel, Stöber process, turbidity, suspension

1. INTRODUCTION

The sol-gel process has been widely used as a very flexible route for the fabrication of silica gel powders in order to produce new porous nanomaterials with well-defined structures, complex shapes and high purity. The sol-gel process was described as relatively simple way, assuming low cost, saving energy, allows the control of the distribution of the component molecules in silica condensed polymers. These materials synthesized by sol-gel method were used for medical science in drug delivery systems [1]. The structural properties of these materials synthesized depend on various experimental parameters (effect of catalyst concentration, pH, etc.). The catalyst concentration and its influence on the silica sols and on the properties of SiO₂ particles have been evaluated for a long time. Stöber et al. [2] reported a pioneering method for synthesizing silica nanoparticles from aqueous alcohol solutions of silicon alkoxides in the presence of ammonia as catalyst. They observed that the silica particles are produced at high concentration of ammonia and small, poly-disperse silica are obtained at low ammonia concentration. Rao and Parvathy [3] have specified that silica gels can only be obtained at 0.01 N concentration of catalyst, while at concentrations higher than 0.01 N, only turbid and opaque colloid solutions (sols) arise. This result may be explained by the interaction of TEOS with the catalyst (ammonia) strongly influenced by synthesis and processing parameters. Fardad [4] studied the role of different catalysts, including ammonia at two different concentrations of 0.01M and 0.001M. At these concentrations the silica sol became translucent and large particles were formed at the end. Ibrahim and al. [5] prepared the silica spherical particles in which was studied the effect of catalyst concentration (NH₃) on the silica particles size. They observed that the silica particles increasing with catalyst (NH₃) concentration in the range 0.11÷0.3 M. Sumathi and al. [6] synthesizing the silica spherical particles, by using sol-gel method. They investigated the role of catalyst concentration on the small size of silica particles at low concentrations. With the increase in the amount of NH₃, the size of particles gradually increased and produces irregular spherical particles with high aggregation effect.

It has to be clearly explained that to our best knowledge, all previously reported experiments dealing with the influence of pH or catalyst concentration on the sol-gel process and/or upon the resulted nanomaterials properties, were based on the study of sample series prepared at alcoxide precursor (TEOS): catalyst (NH₃) variable molar ratio.

In the present work has been described the influence of catalyst, NH₃ (by measuring pH) on the silica suspension and silica structural parameters (surface area, porosity, shape and size) following a different rule. Specifically, it was established the reaction mixture molar ratios, including alcoxide: NH₃ one that was kept constant in all samples. Stable (no gelling) silica sols and solid silica particles were obtained under different basic and stirring conditions.

The aim of paper was the synthesis and characterization of silica particles and colloids by sol-gel process non-assisted (mechanic stirring) and assisted by ultrasonic field (20 kHz ultrasonic bath). Ammonia solution with different concentrations, obtained by successive dilutions, were supplied which clearly influenced the suspension stability and silica morphology. By only varying the concentration of catalyst added solution we can get the control on the silica hydrolysis and condensation process and therefore over structural properties of the synthesized silica. All the concentrations of ammonia mentioned in paper were calculated in relation to the total amount of water brought into the system that was kept rigorously constant. It has been noted once again, the molar ratio TEOS: H₂O: NH₃, for overall process, was also rigorously kept constant.

2. METHOD

Experimental Method

BET surface areas and BJH pore size were determined from N₂ adsorption/desorption isotherm at 77 K using a Quantachrome Nova 1200e instrument. Degassing of the samples in vacuum for 4 hours at room temperature (298 K) precede every measurement;

Pore volumes were calculated from the last point of adsorption isotherm; pore diameters were calculated by Barrett-Joyner-Halenda (BJH) method from the adsorption/desorption branches of the isotherms using a NovaWin software;

The morphological characterization of the samples was done by using Scanning Electron Microscopy (SEM). For SEM an INSPECT S (FEI Company, Holland) instrument has been used;

FT-IR spectra were carried out as KBr pellets, in the 4000-400 cm⁻¹ range on JASCO 430 apparatus.

3. Results and Discussions

Silica nanoparticles were synthesized in two ways, following the Stöber process and keeping the same molar ratio of reactants TEOS: H₂O: ETOH: NH₃ 1: 25: 20: 0.003 **0.2**. For the first series, mechanical stirring route was used and xerogels were obtained. The second series were realized by sono-catalyzed sol-gel process, keeping all the process parameters at the same regime and sonogels were obtained. Total NH₃ amount in the reactants mixture was kept constant and ammonium supplied solutions concentrations were varied on the expenses of water amount calculated for a value of 25 (mole H₂O:mole TEOS).

The synthesis parameters are presented in the Table 1 and rigorously kept constant.

Table 1: The molar ratio of reactants TEOS: H₂O: ETOH: NH₃ 1: 25: 20: 0.2

Samples		TEOS [Mol]	Water* [Mol]	ETOH [Mol]	NH ₃ [mol]	NH ₃ solution [%]
Xerogels	Sonogels					
S1P1	S2P1	1	25	20	0.2	25%
S1P2	S2P2	1	25	20	0.2	12%
S1P3	S2P3	1	25	20	0.2	6%
S1P4	S2P4	1	25	20	0.2	3%

*Total water amount was kept constant related to variable ammonium supplied solution concentrations

It was prepared two series of samples, each one being composed of four samples. For the first series (classic sol-gel route), the S1P1 sample was prepared by adding 0.23 ml solution of 25%NH₃. The second sample, S1P2, was prepared by adding 0.46 ml of solution 12%NH₃

and so forth, the following 2 samples, S1P3 and S1P4, were prepared by supplying further diluted ammonia solutions of 6%NH₃ and 3%NH₃ respectively.

The sonoactivated series of samples was prepared by following the same procedure except supplementary treatment in ultrasonic field in described conditions. For the second series (ultrasonic bath), the S2P1 sample was prepared by adding 0.23 mL solution of 25%NH₃. The following samples S2P2, S2P3 and S2P4 were made by successive dilutions of 12%NH₃, 6%NH₃ and 3%NH₃ supplying ammonia solution concentration. The way, in which synthesis has been achieved, amount of reactants, was revealed in the Table 2.

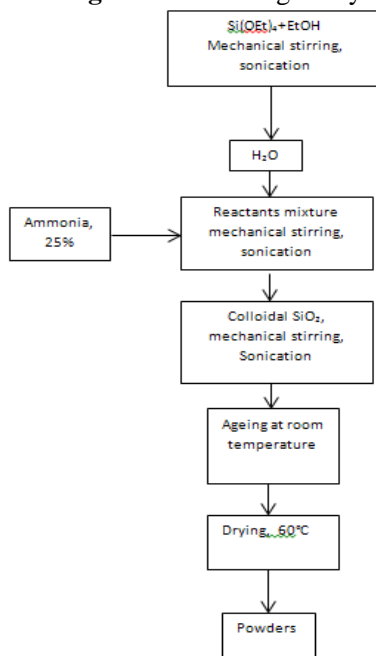
Table 2: The synthesis parameters

Samples		TEOS [mL]	Water [mL]	ETOH [mL]	NH ₃ [mL]	*NH ₃ solution [%]	pH _{NH₃} solution
Xerogels	Sonogels						
S1P1	S2P1	3.5	6.89	18.6	0.23	25%	12
S1P2	S2P2	3.5	6.60	18.6	0.45	12%	11
S1P3	S2P3	3.5	6.15	18.6	0.9	6%	10.5
S1P4	S2P4	3.5	5.25	18.6	1.8	3%	10.5

*NH₃ solutions added were diluted on account of water added to the system TEOS-H₂O-ETOH-NH₃

The main steps of xerogels and sonogels synthesis technology are presented in Figure 1.

Figure 1 Technological synthesis

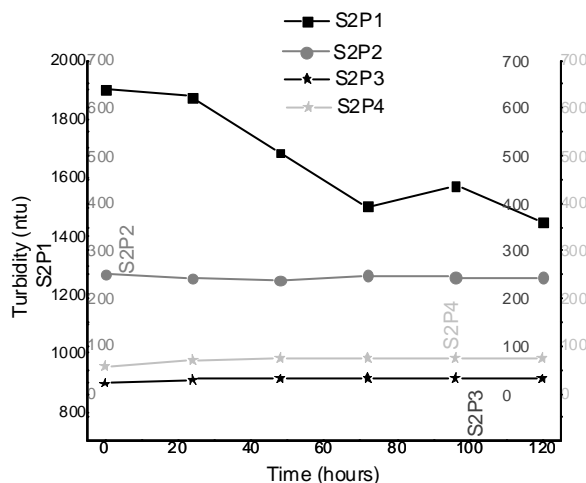


We systematically have examined the influence of adding the base solutions at different concentrations, specific, 25%, 12%, 6%, 3%NH₃, upon the silica sol stability and also upon

the resulted silica xerogel and sonogel samples properties. More or less stable colloidal suspensions and/or precipitates were obtained. The xerogels/sonogels turbidity was measured.

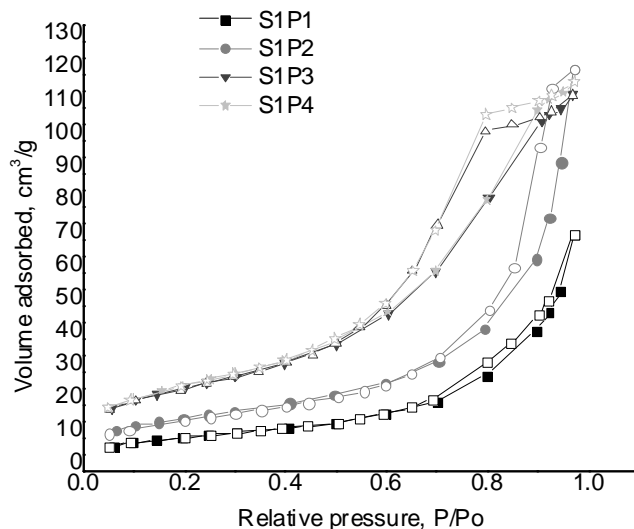
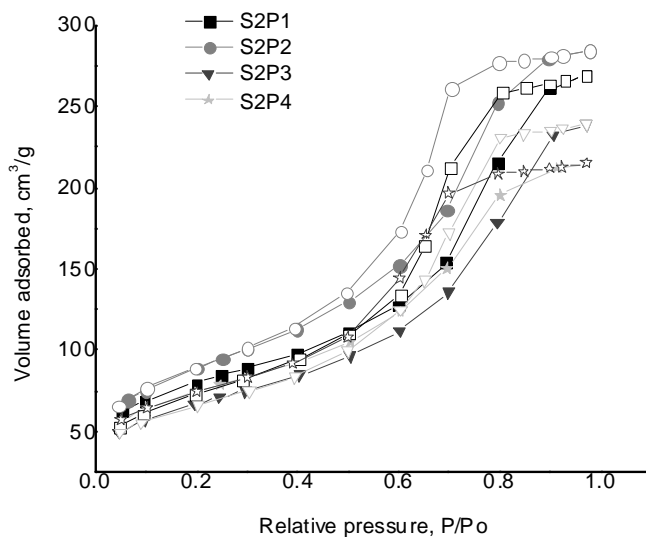
The sonogels kept their stability over the time. The evolution of sonogels stability was exhibited in Figure 2.

Figure 2 Turbidity evolutions over time



24 hours after synthesis, it could be observed that for the sample with the highest concentration of ammonia solution, S2P1 (25% NH_3), nucleation and growth phase occurred by Ostwald Ripening. After 72 hours the flocculation, the particles will be attracted by Van der Waals forces, aggregation begins. This was suggested that the colloidal system is an emulsion the droplets will coalesce, and also increasing the value of turbidity. The decreased value of turbidity after 96 hours indicated that deposition of particles occurred. The same phenomenon took place for the sample S2P2 (12% NH_3), nucleation (growth) – flocculation – aggregation – deposition. The smallest and constant values in time of the turbidity were for the samples treated with lower supplying NH_3 solution concentrations, namely S2P3 (6% NH_3) and S2P4 (3% NH_3), showed that particles deposition never occurred, remain translucent/transparent and kept the stability over the time.

The structural characterization of silica xerogels were carried out using BET [7] surface area analyser (Quantachrome Nova 1200e) at 77K. N_2 adsorption/desorption isotherms over a range of relative pressure P/P_0 from 0.05÷0.1 were collected for all samples. Specific surface areas were determined from the BET equation at a relative pressure range between 0.05÷0.1. The total pore volume was calculated from the last point of adsorption isotherm. Pore size was calculated with the equation $(D) = \frac{4V_p}{S_p \cdot d_{\text{SiO}_2}}$, where $d_{\text{SiO}_2} = 2.2 \text{ g/cm}^3$ [8]. The N_2 adsorption/desorption isotherms are presented in Figure 3a) and Figure 3b).

Figure 3a) N₂ adsorption/desorption xerogel's isotherms**Figure 3b)** N₂ adsorption/desorption sonogel's isotherms

Both silica series exhibited Type IV isotherm with H2 and H3 hysteresis loop according to IUPAC classification which is characteristic for mesoporous solids [9]. In Figure 3a) the adsorption/desorption isotherms for xerogels were presented. After BDDT classification [10], the N₂ adsorption/desorption isotherms were type IV, that are typically for mesoporous materials. The N₂ adsorption/desorption isotherms present different types of hysteresis loop, due to the capillary condensation taking place in the mesopores. The xerogels S1P1 (25% NH₃) and S1P2 (12% NH₃) indicate a type H3 hysteresis loop, according to IUPAC classification [9]. At the relative pressure range of 0.6 P/Po, the H3 hysteresis loop was attributed to the inter-particle porosity distance. Usually, these types of hysteresis loop owe

their shape to presence of aggregates, giving rise to slit-shaped pores [9]. The samples S1P3 (6%NH₃), S1P4 (3%NH₃) indicate a type H2 hysteresis loop which was explained as a consequence of the inter-connectivity of pores – “ink bottle” pores [11].

Figure 3b) shows the N₂ adsorption/desorption isotherm for the samples under ultrasonic field action. The N₂ adsorption/desorption isotherm shows a typical IUPAC type IV [9] pattern with sharp inflection of nitrogen adsorbed volume at P/P₀ about 0.4, with an H2 hysteresis loop [9], suggesting the existence of mesopores with an interconnected pores network of different shapes and sizes. From N₂ adsorption/desorption isotherms were derived the textural parameters of xerogels/sonogels. In Table 3 and Table 4 are presented the textural-parameters for xerogels and sonogels series.

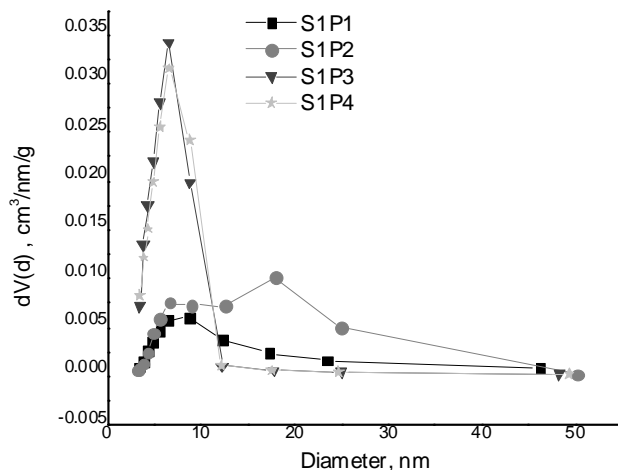
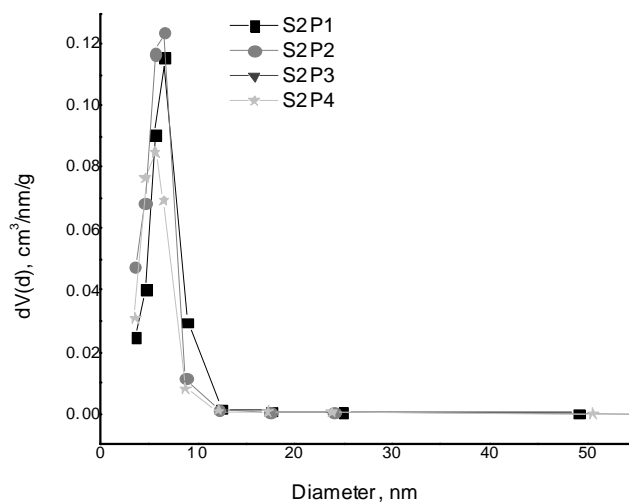
Table 3 Xerogels texturals parameters

Xerogels	Pore diameter (BJH Ads.) [nm]	Pore diameter (BJH Des.) [nm]	Surface area (BET) [m ² /g]	Total pore volume [cm ³ /g]	Particle size [nm]
S1P1(25%NH ₃)	8.83	8.77	36	0.11	74
S1P2(12% NH ₃)	6.15	17.92	56	0.18	48
S1P3(6% NH ₃)	6.16	6.59	89	0.17	30
S1P4(3%NH ₃)	6.14	6.55	92	0.18	29

Table 4: Sonogels texturals parameters

Sonogels	Pore diameter (BJH Ads.) [nm]	Pore diameter (BJH Des.) [nm]	Surface area (BET) [m ² /g]	Total pore volume [cm ³ /g]	Particle size [nm]
S2P1(25%NH ₃)	8.68	6.62	275	0.41	9.9
S2P2(12% NH ₃)	8.74	6.65	314	0.44	8.6
S2P3(6% NH ₃)	6.16	6.58	235	0.37	11.5
S2P4(3%NH ₃)	6.14	5.68	257	0.33	10.5

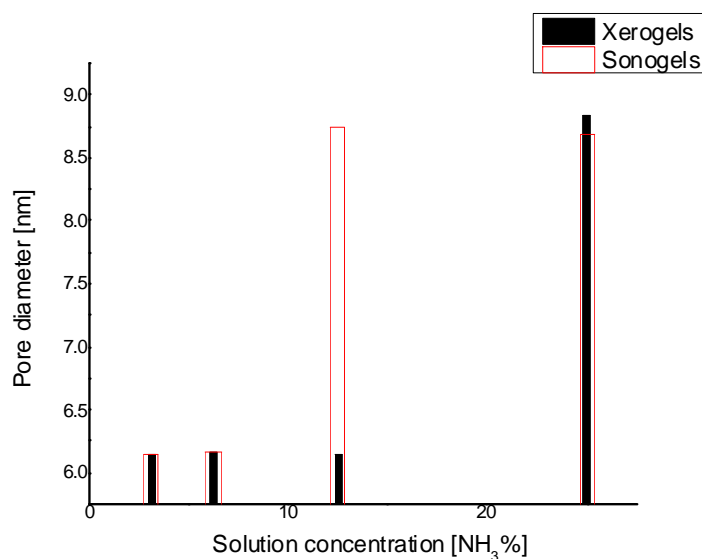
Supplementary information on the effects of supplied ammonia solution concentration on the gels structure can be remarked from the pores size distribution. In figure 4a) and Figure 4b) are represented the pores size distributions for both series.

Figure 4a) Xerogels size distribution**Figure 4b)** Sonogels size distribution

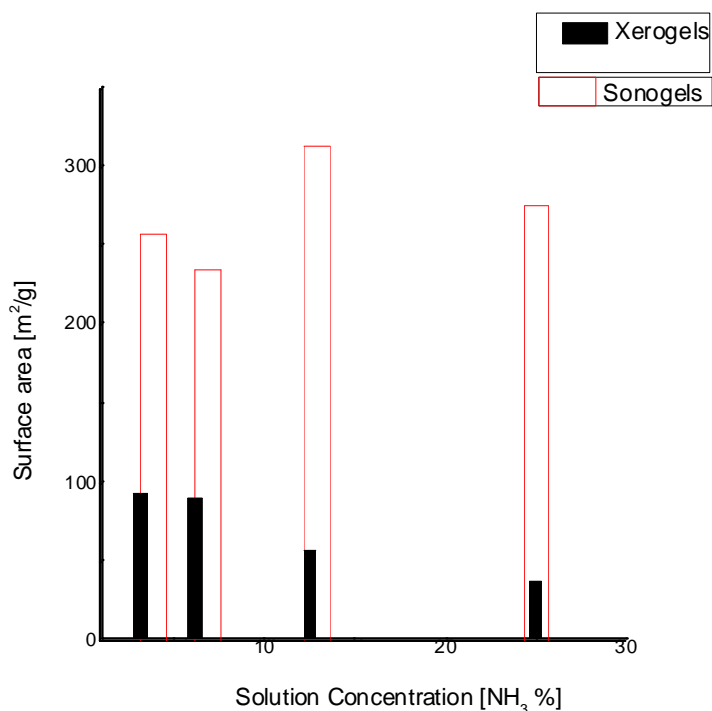
From Figure 4a), the xerogels presented a large pore size distribution in the domain 2-50 nm that was characteristic for mesoporous materials. Xerogels obtained by decreasing ammonia solution concentration, namely S1P1 and S1P2 exhibit a wide pore distribution related to xerogels with small concentration where the pore distribution was narrower, specifically the samples S1P3, S1P4 where the pore diameter was around of 7 nm). The sample S1P2 has a bimodal distribution with two maxim peaks around 7 nm and 20 nm.

From Figure 4b) it can be seen that in the case of sonogels, the pore size distribution was narrower and centred in the domain 2-10 nm, where the most pores were found. A correlation of textural parameters (pores diameter, surface area, and pores volume, particles size) was attempted with the concentration of ammonia solution. Figure 5 it showed the variation of pore diameter related to supplied NH_3 solution concentration for both series of xerogels/sonogels series.

Figure 5 Pore diameter related to ammonia solution



For both series, from adsorption/desorption isotherm it can be seen that by increasing the ammonia supplied solution concentration leads to the higher pore diameters. From desorption isotherm branch we can not have a clear orientation for xerogels because the sample S1P2 has an out of range value (12% S1P2 17.92 nm). From adsorption isotherm branch it can be seen that the pore diameter increase with supplying NH_3 solution concentration, the highest value was obtained for 25% S1P1 (~8.8 nm). It has to be noted that the average particle diameters of sonicated series are considerably smaller and they present a narrower distribution. The value of pore diameter for both series was 6-9 nm (from adsorption branch). In Figure 6 was represented the surface area correlated with supplied ammonia solution for both xerogels/sonogels series.

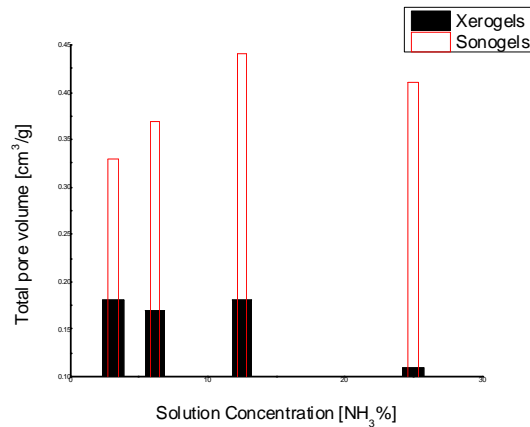
Figure 6 Surface area related to ammonia solution

From Figure 6, it can be seen that in the case of xerogels series, the highest surface area of 92 m²/g, corresponding to the most diluted catalyst supplied solution, S1P4 (3% NH₃). Within the xerogel series, surface area presented a continuous increased tendency as supplied ammonia was more diluted. The sample S1P1 (25% NH₃) has the smallest surface area (36 m²/g). In the case of the sonicated series, first of all, it was observed that surface areas significantly increased. By using supplied ammonia solution concentration of 12% NH₃, the highest surface area that was obtained, 314m²/g.

In Figure 7 was exhibit the correlation between the xerogels/sonogels total pore volumes related to supplied NH₃ solution concentration.

From Figure 7 it can be seen that in the case of xerogels series the catalyst dilution was most favourable in order to increase the total pore volume. In the case of sonicated series of samples, the highest total pore volume (0.44cm³/g) was obtained for 12% NH₃ concentration of catalyst supplied solution. The total pore volume for entire sonicated series presents significant increased values than that of silica xerogels series.

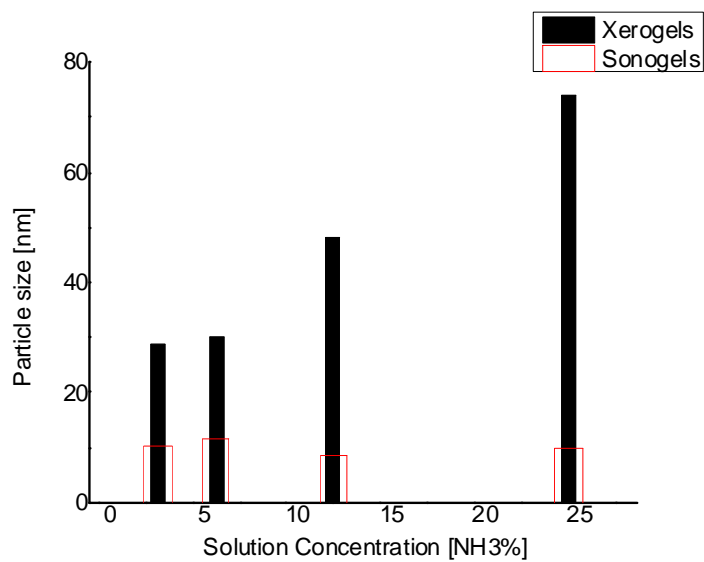
Figure 7 Pore volume related to ammonia solution



Based on N₂ adsorption-desorption isotherms, specifically by using BET technique [7] derived surface area values, the particle size have been calculated with the equation: $(D) = \frac{6}{\rho \cdot S_{BET}}$; where amorphous silica density was, $d_{SiO_2} = 2.2 \text{ g/cm}^3$ [8].

Figure 8 represents the correlation between the particles sizes correlated with the supplying NH₃ solution concentration for both series of samples.

Figure 8 Particle size related to ammonia solution



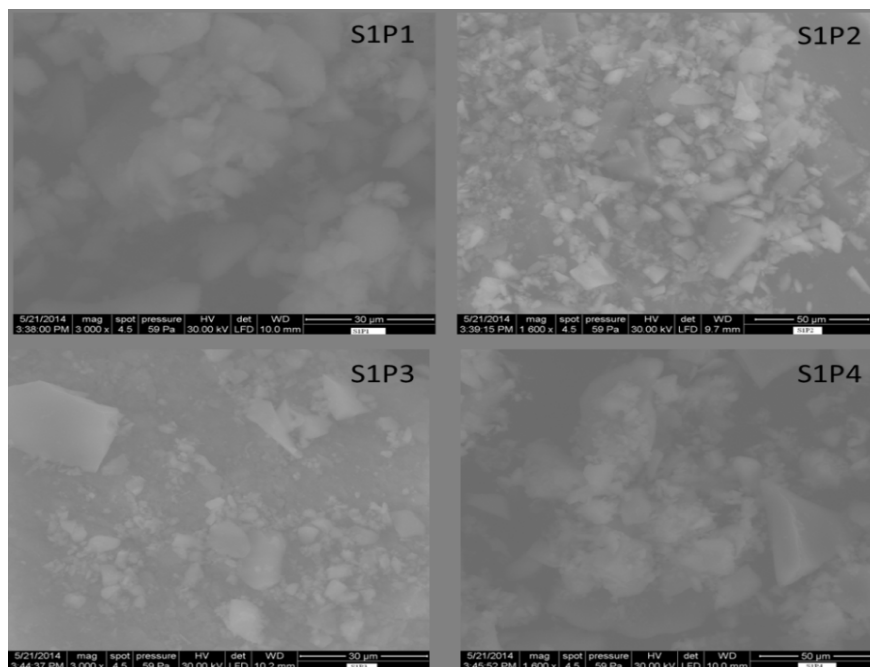
From Figure 8, it can be observed that for xerogels series, particles size significantly decreases with the concentration of supplied NH₃ solution concentration. In the meantime for the sonicated series, particles size has not been significantly influenced by the supplied catalyst solution concentration. A small particles size for sonogels can be observed at critical

concentration of the ammonia (25% NH_3). The particles size decrease with the increasing of ammonia supplying solution concentration. Therefore, for the most concentrated sonogel sample S2P1 (25% NH_3) the particles size was 9.9 nm related to the most diluted sample S2P4 (3% NH_3), where the particles size was 10.5 nm.

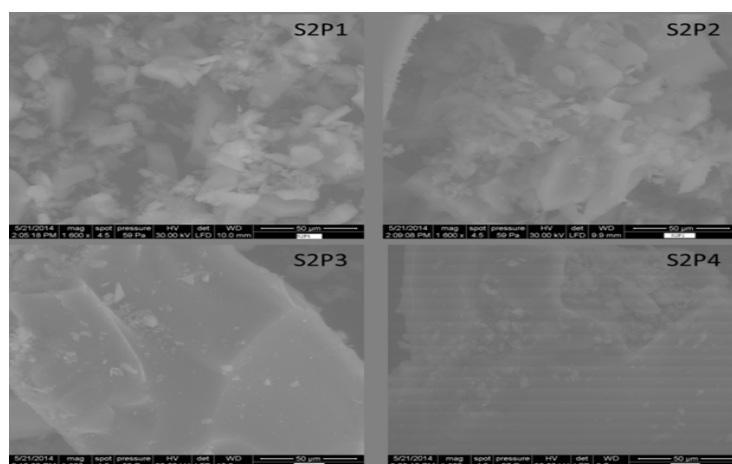
SEM

Figure 9 and Figure 10 shows SEM image of silica xerogels prepared from silica sols with mean particles sizes of ~ 45 nm for xerogels and ~ 10 nm for sonogels. The prepared silica nano-powders show the irregular agglomerated silica particles. The irregular shape of silica particles could be caused by the fast nucleation process, which is difficult to be controlled in alkaline environment [6].

Figure 9 Xerogels SEM image

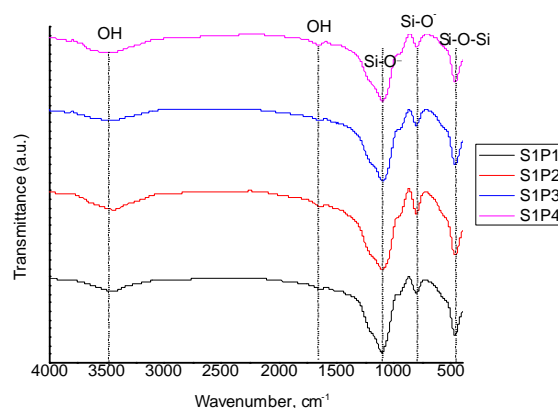


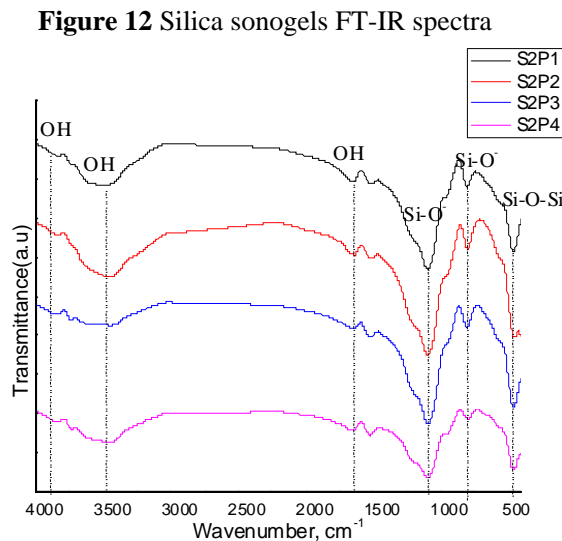
For xerogels, it was observed asymmetrical formations heavily agglomerated. In the case of sonicated samples S2P3 (6% NH_3) and S2P4 (3% NH_3) the SEM images showed a bulk structure.

Figure 10 Sonogels SEM image

FT-IR

In the case of both synthesized samples, at room temperature, the infrared spectra exhibit a broad band at 3400 cm^{-1} due to absorption of bridged hydroxyl group. The broad band from 3400 to 3800 cm^{-1} specifically for sonogels, was ascribed to OH stretching vibrations, bridges between adsorbed water and OH of Si-OH groups or stretching of OH from bridged Si-OH groups [12]. The band due to the bending vibration of molecular water (1640 cm^{-1}) was also present in the FTIR spectra and can be used to study the adsorbed water. The absorption bands at 1093 - 1100 cm^{-1} is attributed to stretching vibration of Si-O bond. The 800 cm^{-1} band corresponding to the ring structure of SiO_4 tetrahedral and the 464 cm^{-1} band correspond to deformation vibration of Si-O-Si [13], [14], [15]. The results of FT-IR spectra were exhibited in Figure 11 and Figure 12.

Figure 11 Silica xerogels FT-IR spectra



4. CONCLUSION

The investigation showed that by keeping rigorously constant all reactants molar ratio TEOS: H₂O: ETOH: NH₃ = 1: 25: 20: 0.2 and by supplying different concentrations of NH₃ catalyst, the synthesis outputs changed significantly. The surface area of xerogels was situated up to ~100 m²/g while the sonogels have two-three times higher surface area up to ~300 m²/g. Base concentration by changing pH had the different effects on particles morphology. In case of xerogels and sonogels with the highest ammonia solution concentration it could be seen a more porous structure, due to the formation of particles (depositing of precipitated particles in solutions). For all concentrations of ammonia solution silica precipitates were obtained, by classic sol-gel process and relatively stable translucent silica colloids, under ultrasonic field action. Pore size distribution for sonogels was significantly narrower (~6-9 nm). The sizes of silica colloids decreases with increasing the ammonia concentrations, the number of nuclei was larger and therefore smaller silica colloids are obtained. In the case of highest ammonia catalyst (25%NH₃), larger particles precipitated, so that the formation of a stable suspension of silica particles was not possible to form because the nucleation process produced primary particles nuclei and therefore larger silica particle size was formed. At high pH values, where the particles may have a high solubility in the sol, more porous structures are obtained, the particle sizes increases. SEM image reveals that the particles start to agglomerate in the alkaline media (NH₃); it was observed that the structure start to modifying leading to irregular silica shapes. From FTIR spectra has been shown that all xerogels/sonogels samples presented silica similar bands corresponding to -OH and -Si-O groups. The SiO₂ particles size was found to increase with ammonia concentration up to 0.01 M (NH₃ 25%), for ammonia concentration under 0.01 M, the particles size decrease.

ACKNOWLEDGEMENT(S)

Authors thanks to Romanian Academy.

REFERENCES

- 1) Liberman, A.; Mendez, N., Trogler, W.C., Kummel, A.C., Synthesis and surface functionalization of silica nanoparticles for nanomedicine, *Surf Sci. Rep.*, **2014**, 69, 132-158.
- 2) Stober, W.; Fink, A., Bohn, E., Controlled Growth of Monodisperse Silica Spheres in the Micron Size Range, *J. Colloid Interface Sci.*, **1968**, 26, 62-69.
- 3) Rao, A.V.; Parvathy, N.N., Effect of Gel Parameters on Monolithicity and Density of Silica Aerogels, *J. Mater. Sci.*, **1993**, 28, 3021–3026.
- 4) Fardad, M.A., Catalysts and the structure of SiO₂ sol-gel films, *J. Mater. Sci.*, **2000**, 35, 1835-1841.
- 5) Ibrahim, A.M.I.; Zikry, A.A.F, Sharaf, M.A., Preparation of spherical silica nanoparticles: Stoeber silica, *J. Am. Sci.*, **2010**, 6, 11.
- 6) Sumathi, R.; Thenmozhi, R., Synthesis and Characterization of Spherical Silica Nanoparticles by Sol-Gel Method, *International Conference on Systems, Science, Control, Communication, Engineering and Technology (ICSSCCET)*, **2015**, 204-208.
- 7) Brunauer, S.; Emmett, PH., Teller E., Gases in multimolecular layers, *J. Am. Chem. Soc.*, **1938**, 60, 309–319.
- 8) Sun, S.; Zeng, H., Size-Controlled Synthesis of Magnetite Nanoparticles. *J. Am. Chem. Soc.*, **2002**, 124, 8204–8205.
- 9) Sing, K. S. W.; Everett, D.H., Haul, R.A.W., Moscou, L., Pierotti, R.A., Rouquerol, J., Siemienewska, T., *Reporting Physisorption Data For Gas Solid Systems, Pure Appl. Chem.*, **1985**, 57, 603-619.
- 10) Brunauer, S.; Deming, L.W., Teller, E., *J. Am. Chem. Soc.*, **1940**, 62, 1723.
- 11) McBain, J. W., *J. Am. Chem. Soc.*, **1935**, 57, 699.
- 12) Ying, J.Y.; Benziger, J.B., Navrotsky, A. Structural Evolution of Alkoxide Silica Gels to Glass: Effect of Catalyst pH, *J. Am. Ceram. Soc.*, **1993**, 76, 2571-2582.
- 13) Kamistos, E.I.; Patsis, A.P., Chryssikos, G.D., *J. Non- Cryst. Solid*, **1993**, 152, 246.
- 14) Wood, D.L.; Rabinovich, E.M., *Appl. Spectrosc.*, **1989**, 43, 263.
- 15) Costa, T. M. H.; Gallas, M.R., Benvenuti E.V., da Jornada J. A. H., Infrared and Thermogravimetric Study of High Pressure Consolidation in Alkoxide Silica Gel Powders, *J. Non-Cryst. Solids*, **1997**, 220, 195-201.

Letter

THE EFFECTS OF IONS IN AMNIOTIC FLUID IN DEVELOPMENT OF FETUS

Radu Neamtu^{(1),(*)}, **Ion Neamtu**⁽²⁾, **Andrei Motoc**⁽³⁾

1 University of Medicine and Pharmacy Timisoara, Romania;

2 University “Titu Maiorescu” Bucuresti, Romania;

3 University of Medicine and Pharmacy Timisoara, Romania

ABSTRACT

The amount of amniotic fluid increases steadily to reach a maximum of approximately 400-1200 ml at 34-38 weeks, and then subsequently starts declining. At 40 weeks, the volume of amniotic fluid is approximately 800 ml (1,2,3) and continues to decrease till the pregnancy continues.

The composition of amniotic fluid changes with time and does not remain constant throughout pregnancy (4). It comprises of not only water, which forms around 98-99% of the amniotic fluid, but also several other essential constituents

Keywords: amniotic fluid, ions, pregnancy

1. INTRODUCTION

There is not much literature available on the ionic composition of amniotic fluid. Although electrolytes are present in the amniotic fluid in trace amounts, they are considered essential for the health and well-being of the fetus. Multiple researchers have shown the correlation between amniotic fluid electrolyte concentrations and fetal development (5). The common ions found in amniotic fluid include sodium, potassium, chloride, calcium, magnesium, and bicarbonate (6). Knowledge of the role of these ions in the amniotic fluid in a normal pregnancy can aid in prevention and early diagnosis of fetal or maternal pathologies. By accurate prenatal assessment of the biochemical composition of the amniotic fluid, one

* Correspondent author: Tel:+40729098886, E-mail: neamturaduionut@gmail.com

can evaluate fetal maturity and overall health status. This paper thus aims at assessing the function of these ions in amniotic fluid on fetal growth and development, based on the current, available literature.

2. FORMATION OF AMNIOTIC FLUID

Almost at the same time as the implantation, an extracolemic cavity is produced that forms the amniotic space (4). During the entire pregnancy, the growing fetus and amniotic fluid are both enveloped in the amniotic sac. Initially, the maternal plasma mainly contributes to the formation of the amniotic fluid and reaches the fetus by traversing the fetal membranes. However, as the placenta is formed, the plasma from the mother's blood crosses the placenta and reaches the fetus, contributing to the amniotic fluid. As the fetal skin is not keratinized in early pregnancy, there is diffusion of amniotic fluid across the fetal skin, and it is similar in composition to the plasma of the fetus. However, post-keratinization of the fetal skin, the absorption of the fluid takes place through the fetal gut.

3. COMPOSITION OF AMNIOTIC FLUID

The composition of amniotic fluid changes with time and does not remain constant throughout pregnancy (4). It comprises of not only water, which forms around 98-99% of the amniotic fluid, but also several other essential constituents.

Sodium

Several studies have documented the decrease in amniotic fluid sodium levels with gestational age (7). Sodium is involved in the regulation of water-electrolyte balance of the amniotic fluid and is thus an important ion in the amniotic fluid. Even a small change in the sodium ion concentrations can lead to significant changes in the volume of amniotic fluid (8).

Additionally, a study carried out on sheep showed that chronic placental insufficiency led to an increase in sodium ion concentration with a decrease in amniotic fluid volume (9).

Chloride

Although chloride levels fall as the pregnancy progresses, the decline is minimal as compared to other ions such as sodium (10).

Since the amniotic fluid is mainly composed of fetal urine in the latter part of pregnancy, any renal pathology will affect the amniotic fluid composition. Bartter syndrome is one such

disorder that can be diagnosed prenatally by detecting high chloride levels in the amniotic fluid (11).

Potassium

The concentration of potassium ions in the amniotic fluid is found to be almost constant throughout pregnancy (12-14). Raised potassium levels in amniotic fluid have been reported in women suffering from preeclampsia (15). Moreover, a study compared the concentration of trace elements in amniotic fluid, with their antibacterial activity (16). This study assessed the amniotic fluids of 39 pregnant women in their second half of pregnancy and revealed that lower concentrations of potassium were associated with good antibacterial activity.

Calcium

Cruikshank *et al* demonstrated the change in calcium ion levels in amniotic fluid along with the levels of calcium regulating hormones, as the pregnancy progresses (17). Their study showed that though the total calcium levels fall progressively, the levels of ionized calcium remains almost constant.

Low calcium levels in amniotic fluid have found to be associated with preterm deliveries (18).

On assessment of pregnancies complicated by spina bifida, it was found that they show a high level of calcium ions in the amniotic fluid (19).

An increased level of calcium and other bivalent cations such as zinc has also been observed in women suffering from preeclampsia (20). It is hypothesized that this is possibly due to reduced maternal excretion, leading to increased fetal load.

Magnesium

A study was carried out in 2011 (21) with the aim to determine the level of magnesium in amniotic fluid in the second trimester of pregnancy. According to this study, the mean magnesium value in amniotic fluid was 1.65 ± 0.16 mg/dL and slightly more, at 1.97 ± 0.23 mg/dL in serum.

The role of magnesium in amniotic fluid has been highlighted in several studies. Low levels of magnesium in amniotic fluid have been associated with preeclampsia (22) and diabetes (23, 24). However, some studies point to the contrary showing raised levels of magnesium ions in the amniotic fluid of patients with preeclampsia (20).

Pregnant women need magnesium supplementation in their diet due to the reduced serum levels during pregnancy (25,26).

Bicarbonate

A study that evaluated the amniotic fluid composition in a pregnancy complicated with twin-twin transfusion syndrome found that in comparison with the normal pregnancies, the complicated pregnancies showed a higher bicarbonate levels in the amniotic fluid (27).

Zinc

Like magnesium, zinc deficiency has also been implicated in fetal growth retardation. A decrease in zinc levels in amniotic fluid has shown association with intrauterine growth retardation resulting from placental insufficiency (28).

Zinc is also associated with antibacterial activity in the amniotic fluid. Scane *et al* demonstrated that both high and low molecular-weight antibacterial activity was directly related to the concentration of bound zinc (29). This collaborates with the present evidence stating the importance of zinc in the regulation of several aspects of the immune system. (30).

REFERENCES

1. Brace R, Wolf E. Normal amniotic fluid volume changes throughout pregnancy. *Am J Obstet Gynecol.* 1989;161(2):382-388.
2. Elliott PM, Inman WH. Volume of liquor amnii in normal and abnormal pregnancy. *The Lancet.* 1961;278(7207):835-840.
3. Queenan J, Thompson W, Whitfield C, Shah S. Amniotic fluid volumes in normal pregnancies. *Am J Obstet Gynecol.* 1972;114(1):34-38.
4. Underwood M, Gilbert W, Sherman M. Amniotic Fluid: Not Just Fetal Urine Anymore. *J Perinatol.* 2005;25(5):341-348.
5. Cassady G, Barnett R. Amniotic fluid electrolytes and perinatal outcome. *Neonatology.* 1968;13(3-4):155-174.
6. Lind T, Billewicz W, Cheyne G. Composition of amniotic fluid and maternal blood through pregnancy. *BJOG.* 1971;78(6):505-512.
7. Leela KV, Babu K. Study of biochemical parameters in amniotic fluid for assessment of foetal maturity in cases of normal pregnancy. *J of Evidence Based Med & Hlthcar.* 2016;3(3):8394-8399.
8. Curran M, Nijland M, Mann S, Ross M. Human amniotic fluid mathematical model: Determination and effect of intramembranous sodium flux. *Am J Obstet Gynecol.* 1998;178(3):484-490.
9. Gagnon R, Harding R, Brace R. Amniotic fluid and fetal urinary responses to severe placental insufficiency in sheep. *Am J Obstet Gynecol.* 2002;186(5):1076-1084.
10. Sieck UV, Ohlsson A. Fetal polyuria and hydramnios associated with Bartter's syndrome. *Obstet Gynecol.* 1984;63:22S-24S.
11. Massa G, Proesmans W, Devlieger H, Vandenberghe K, Van Assche A, Eggermont E. Electrolyte composition of the amniotic fluid in Bartter syndrome. *Eur J Obstet Gynecol Reprod Biol.* 1987;24(4):335-340.
12. Lind T. The biochemistry of amniotic fluid. In: Sandler M, ed. *Amniotic fluid and its clinical significance.* New York: Marcel Dekker Inc, 1981; pp. 1-25.
13. Benzie RJ, Doran TA, Harkins JL, Owen VM, Porter CJ. Composition of the amniotic fluid and maternal serum in pregnancy. *Am J Obstet Gynecol.* 1974;119:798-810.

14. Gillibrand P. Changes in the electrolytes, urea and osmolality of the amniotic fluid with advancing pregnancy. *J Obstet Gynaecol Br Commonw.* 1969;76(10):898-905.
15. Fotiou M, Michaelidou A, Masoura S, Menexes G, Koulourida V, Biliaderis C, et al. Second trimester amniotic fluid uric acid, potassium, and cysteine to methionine ratio levels as possible signs of early preeclampsia: A case report. *Taiwan J Obstet Gynecol.* 2016;55(6):874-876.
16. Honkonen E, Nántö V, Hyörä H, Vuorinen K, Erkkola R. Trace elements and antibacterial activity in amniotic fluid. *Neonatology.* 1986;50(1):21-26.
17. Cruikshank D, Pitkin R, Williams G, Hargis G, Reynolds W. Calcium-regulating hormones and ions in amniotic fluid. *Am J Obstet Gynecol.* 1980;136(5):621-625.
18. Shah M, Modi U, Bhatt R, Mistry K. Amniotic fluid composition in abnormal pregnancies. *Indian J Pediatr.* 1983;50(3):271-274.
19. Pettit B, Baker S, King G. The composition of amniotic fluid in pregnancies complicated by fetal anencephaly or spina bifida. *Br J Obstet Gynaecol.* 1979;86(8):637-641.
20. Weiss M, Frenkel Y, Dolev E, Barkai G, Mashiach S, Sela B. Increased amniotic fluid divalent cation concentrations in preeclampsia. *J Basic Clin Physiol Pharmacol.* 1995;6(1).
21. Bocos Terraz J, Izquierdo Álvarez S, Bancalero Flores J, González López Á, Escanero Marcén J. Magnesium concentration in amniotic fluid in the early weeks of the second trimester of pregnancy. *BMC Res Notes.* 2011;4(1):185.
22. Dawson E, Evans D, Nosovitch J. Third-trimester amniotic fluid metal levels associated with preeclampsia. *Arch Environ Health.* 1999;54(6):412-415.
23. Mimouni F, Miodovnik M, Tsang RC, Caliahan J, Shaul P. Decreased amniotic fluid magnesium concentration in diabetic pregnancy. *Obstet Gynecol.* 1987;69:12-14.
24. Doraczynska E, Rechberger T, Wawrzycka B, Oleszczuk J. Concentration of magnesium in the amniotic fluid of a patient with diabetes. *Ginekol Pol.* 1995;66:653-655.
25. Gortzak-Uzan L, Mezad D, Smolin A, Friger M, Huleihel M, Hallak M. Increasing amniotic fluid magnesium concentrations with stable maternal serum levels: a prospective clinical trial. *J Reprod Med* 2005;50:817-820.
26. Chazan B, Kowaiska B, Pietrasik D, Jarosz I. Effect of vitamin/mineral supplementation on calcium, magnesium and iron levels in amniotic fluid and serum taken from during first half of pregnancy. *Ginekol Pol.* 2001;72:993-996.
27. Adama van Scheltema P, In't Anker P, Vereecken A, Vandenbussche F, Kanhai H, Devlieger R. Biochemical composition of amniotic fluid in pregnancies complicated with twin-twin transfusion syndrome. *Fetal Diagn Ther.* 2005;20(3):186-189.
28. Pogorelova T, Linde V, Gunko V, Selyutina S. The imbalance of metal-containing proteins and free metal ions in the amniotic fluid during fetal growth. *Biomed Khim.* 2016;62(1):69-72.
29. Scane T, Hawkins D. Antibacterial activity in human amniotic fluid: relationship to zinc and phosphate. *Br J Obstet Gynaecol.* 1984;91(4):342-348.
30. Shankar AH, Prasad AS. Zinc and immune function: the biological basis of altered resistance to infection. *Am J Clin Nutr.* 1998;68(2 Suppl):447S-463S.

Review

ELECTROCHEMICAL SYSTEMS AND MECHANICALLY INTERLOCKED MOLECULES. PART 1: NANOSCIENCE

Mirela I. Iorga (1,2), Marius C. Mirica (1) and Mihai V. Putz (1,2, *)

1. Laboratory of Renewable Energies-Photovoltaics, R&D National Institute for Electrochemistry and Condensed Matter –INCEMC–Timisoara, Timisoara, Romania
2. Laboratory of Structural and Computational Physical-Chemistry for Nanosciences and QSAR, Biology-Chemistry Department, West University of Timisoara, Timisoara, Romania

ABSTRACT

The aim is to re-dimension More's law in nano-chemical devices by modelling quasi-particle couplings (bondonic and bondotic) as QBits impulses on chemical-physical nano-compounds (graphene lattices with Stone-Wales rotations topological defects, but also for molecules governed by nano-mechanical chemical bonds) and their propagations as dynamic donors of chemical bond and coupled electron pairs instead of electrons and single atoms as “quantum dots”. This represents the quantum-chemical basis of graphenetrionics (semiconductors, transistors, and integrated circuits based on topological defective graphene) and of photo-activated moletronics (molecular machines). The paper presents the correlation of quantum potentials of electrochemical tunnelling with associated electrochemical currents and with electro-photo-chemical activation mechanism of molecular machines.

Keywords: supramolecular systems, molecular machines, logic gates, graphenetrionics, moletronics.

1. INTRODUCTION

In addition to macroscopic electronic devices in which information processing use electrical signals, the emphasis is now on molecular electronics, the miniaturization of electrical circuits, which can become much smaller than digital circuits manufactured on semiconductor chips [1].

These allow the investigation of the properties of molecules and supramolecular systems, such as electrical conductivity and electrical switching. Supramolecular systems may be

designed to behave like a plug/socket type macroscopic device; they are made of at least two molecular components, which must have two main properties: it must be possible to connect and disconnect the two components reversibly, and when the two elements are connected, the energy or electrons must flow from socket to plug, Figure 1.

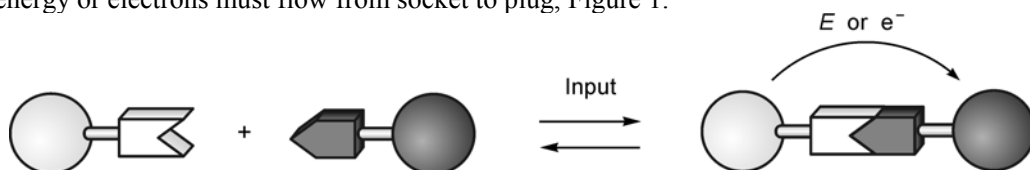


Figure 1. Diagram of a plug-and-socket molecular system [2]

Interactions caused by the hydrogen bonds between ammonium ions and crown ethers have been used profitably, which can be very quickly and reversibly switched on/off by acid-base inputs [2] to develop such types of devices.

Quantum potential barriers

The quantum model of quantum tunnelling electrons in open, dynamic systems is shown in Figure 2.

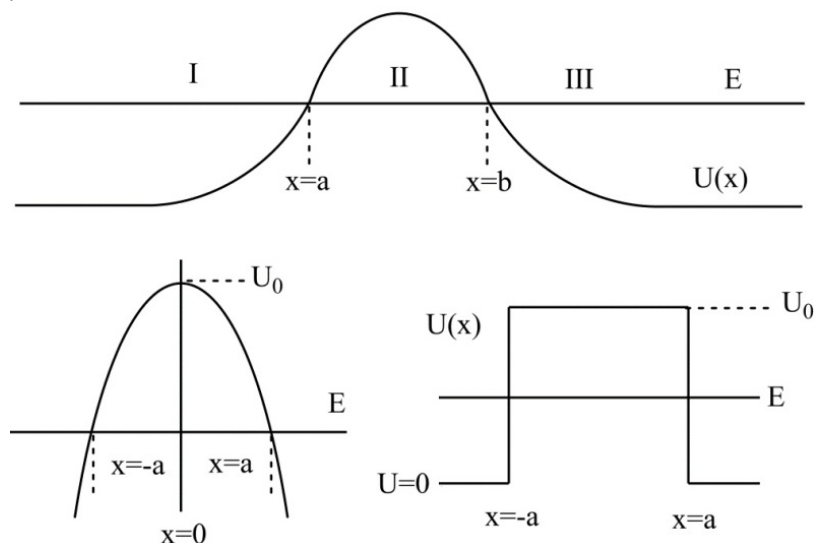


Figure 2. TOP: Lightly rounded potential barrier; BOTTOM-Left: Parabolic Potential Barrier; BOTTOM-right. Rectangular potential barrier (after Bockris & Khan, 1979) [3]

The expression of the total wave function of the global-local information of the system is:
 - for the section I, where $U(x) \cong 0$; $U(x) < E$:

$$\psi_I(x) = \frac{A}{[k(x)]^{\frac{1}{2}}} \exp\left[i \int_a^x k(x) dx\right] + \frac{B}{[k(x)]^{\frac{1}{2}}} \exp\left[-i \int_a^x k(x) dx\right] \quad (1)$$

- for section II where $U(x) > E$:

$$\psi_{II}(x) = \frac{C}{[\kappa(x)]^{\frac{1}{2}}} \exp\left[+ \int_a^x \kappa(x) dx\right] + \frac{D}{[\kappa(x)]^{\frac{1}{2}}} \exp\left[- \int_a^x \kappa(x) dx\right] \quad (2)$$

- for section III where $U(x) < E$:

$$\psi_{III}(x) = \frac{F}{[k(x)]^{\frac{1}{2}}} \exp\left[i \int_b^x k(x) dx\right] + \frac{G}{[k(x)]^{\frac{1}{2}}} \exp\left[-i \int_b^x k(x) dx\right] \quad (3)$$

The correlation between coefficients is:

$$A = \frac{1}{2} \left[F \left(2\theta + \frac{1}{2\theta} \right) + iG \left(2\theta - \frac{1}{2\theta} \right) \right] \quad (4)$$

where:

$$\theta = \exp\left[\int_a^b \kappa(x) dx \right] \quad (5)$$

The transmission coefficient is defined as:

$$P_T = \frac{v_{trans} |\psi_{trans}|^2}{v_{incident} |\psi_{incident}|^2} = \frac{|F|^2}{|A|^2} \quad (6)$$

Because the transmission rate is $v_{trans} = v_{incident}$ and $|A|^2$ is replaced above, the case of WKB approximation (Wentzel-Kramers-Brillouin) will be considered, with the estimation of a large and high barrier, and finally the expression from Eq. (7) will be obtained.

$$P_T = \exp\left(-2 \int_a^b \left\{ \frac{8\pi^2 m}{\eta^2} [U(x) - E] \right\}^{\frac{1}{2}} dx \right) \quad (7)$$

This is the expression of the transmission coefficient using the general expression WKB from the above equation if both the barrier height and width are large. This represents the probability of tunneling, Gamow's equation.

In the case of a parabolic barrier, $U(x) = U_0 - \frac{1}{2}fx^2$ and it has the graphical representation from Figure 2 (Bottom-Left). Then, we will get the expression of the tunneling probability for the parabolic barrier of the form:

$$P_T = \exp\left\{ -\frac{\pi^2 l}{h} [2m(U_0 - E)]^{\frac{1}{2}} \right\} \quad (8)$$

where the barrier width is $l = 2a$ and U_0 represents the maximum of the barrier.

In the case of a rectangular barrier $U(x) = U_0$ and it has the graphical representation from Figure 2 (Bottom-Right), with the tunneling probability of the form:

$$H = \exp\left\{-\frac{4\pi l}{h}[2m(U_0 - E)]^{\frac{1}{2}}\right\} \quad (9)$$

where $l = 2a$ is the thickness or width of the barrier.

Current in quantum electrochemistry

Theoretical modeling of transient experiments in analytical electrochemistry can be achieved through a specific mathematical approach, known as the integral equation method [4]. Bonciocat [5,6] proposes that the equation describing the kinetics of a redox electrode reaction $O + ne^- \leftrightarrow R$ is an integral equation Volterra type (which is a particular case of the integral Fredholm equation), namely:

$$i(t) = \lambda \int_0^t K(t, u) i(u) du + f(t) \quad (10)$$

where: $\lambda = -1$; $i(u)$, $i(t)$: densities of the Faraday currents at time moments $u < t$, respectively t ; $K(t, u)$: the kernel of the integral equation and $f(x)$ have explicit expressions containing the kinetic parameters of the electrode reaction, the concentrations, the diffusion coefficients of the electrochemically active species, the time t , u , the overvoltage at time t (Figure 3).

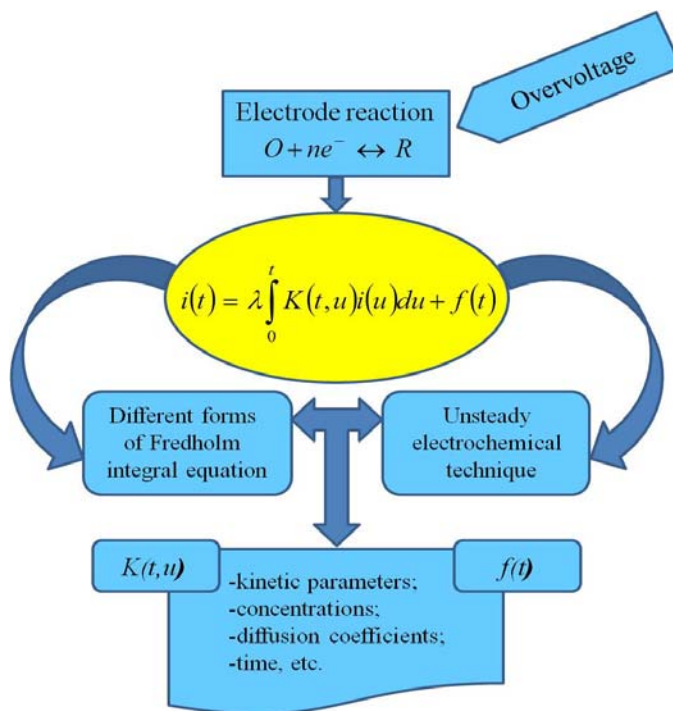


Figure 3. The Fredholm integral algorithm in quantum electrochemistry

By providing the only limitation by charge and mass transfer (by non-stationary diffusion) of these species, the overvoltage $\eta(t)$ applied to the interface is a continuous function on the closed interval $[0, a]$ and both functions $K \cdot(t)$ and $f(t)$ are continuously uniform functions for $t \in [0, a]$.

2. METHOD(S)/MODEL(S)

The original contribution of this paper concerns the development of the following topics:

- Nano-chemistry and multidisciplinary nano-physics;
- Graphene – from the perspective of graphite structured as multi-layer graphene;
- Quantum heterojunctions with graphene;
- Contributions to double-layer quantum electrochemistry;
- Molecular machines in the quantum-electrochemical coupling;
- Prediction of activation energies (possibly of associated micro-currents) with graphenetrionic and moletronic integrated nano-systems.

The specific objectives and the results that will contribute to the achievement of these objectives are as follows: the characterization of “quantum bridges” in electrochemical systems as potentials of tunnelling and photo-electronic activation, the identification of Fredholm integral solutions for electrochemically activated currents, and the selection of quantum-molecular mechanism specific to photo-activation energies in quantum-electrochemical systems with molecular machines.

2.1. Theoretical Method/Model

Potentiostatic Method

In the case of inert metal/redox electrolyte electrodes, by following the application of a constant overvoltage, the electrode response is recorded, which in case of low overvoltages coincides with the density of the faradic current, and the Fredholm equation above becomes:

$$i(t) = \lambda \frac{i^0 N}{\pi^{1/2}} \int_0^t \frac{i(u)}{(t-u)^{1/2}} du - \frac{F}{RT} i^0 \eta \quad (11)$$

Finally, the equation of the potentiostatic method of low overvoltages and times is obtained:

$$i(t) = -\frac{F}{RT} i^0 \eta \left(1 - \frac{2i^0 N}{\pi^{1/2}} t^{1/2} \right) \quad (12)$$

The obtained equations facilitate the determination of the exchange current density i^0 and the kinetic parameters i^{00} and β of the charge transfer reaction, $\ln i^0 = \ln i^{00} c_R^\beta + (1-\beta) \ln c_0$. In the case of an electrode made by inert semiconductor / redox electrolyte, $i_f(t)$ is the density of

the total faradic current, consisting of the contributions of the two energy bands (conduction and valence), according to the equation: $i_F(t) = i_{nF}(t) + i_{pF}(t)$;

If the charge transfer is done only through the conduction band, namely $i_p = 0$, the latest equations become:

$$i(t) = -\frac{F}{RT} i_n^0 \eta \left(1 - \frac{2i_n^0 N}{\pi^{1/2}} t^{1/2} \right), \quad \ln i_n^0 = \ln i_n^{00} c_R^{\alpha_n} + (1 - \alpha_n) \ln c_0 \quad (13)$$

If the charge transfer takes place through both energy bands, the current becomes:

$$i(t) = -\frac{F}{RT} (i_n^0 + i_p^0) P \left(1 - \frac{2(i_n^0 + i_p^0) N}{\pi^{1/2}} t^{1/2} \right) \quad (14)$$

By Eqs. (13) and (14), the sum of the standard densities of the exchange currents through the two energy bands can be obtained.

Galvanostatic method

In case of inert metal/redox electrolyte electrodes, at low overvoltages, the current density in the outer circuit is maintained constant. The sum of the faradic and capacitive components remains constant, although their value changes over time. In this case, the Fredholm equation becomes:

$$i - i_C(t) = \lambda \frac{i^0 N}{\pi^{1/2}} \int_0^t \frac{du}{(t-u)^{1/2}} - \frac{F}{RT} i^0 \eta \quad (15)$$

The equation of the galvanostatic method for low overvoltages is obtained in two cases:

- if the capacitive current is neglected:

$$\eta(t) = -\frac{RT}{F i^0} i \left(1 + \frac{2i^0 N}{\pi^{1/2}} t^{1/2} \right) \quad (16)$$

- if the capacitive current is taken into account:

$$\eta(t) = -\frac{RT}{F i^0} i \left(1 + \frac{2i^0 N}{\pi^{1/2}} t^{1/2} - \frac{RT}{F} N^2 C_d i^0 \right) \quad (17)$$

The obtained equations facilitate the determination of kinetic parameters i^{00} and β of the charge transfer reaction.

Linear Potential Voltammetry

In the case of inert metal/redox electrolyte electrodes, at low overvoltages, the overvoltage applied to the electrode depends on the time and the scanning rate, according to the equation:

$$\eta(t) = \nu t \quad (18)$$

In this case, if the capacitive current is neglected, the Fredholm equation becomes:

$$i = \lambda \frac{i^0 N}{\pi^{1/2}} \int_0^t \frac{i(u)}{(t-u)^{1/2}} du - \frac{Fi^0}{RT} vt \quad (19)$$

and if the capacitive current cannot be ignored, the Fredholm equation will be:

$$i = \lambda \frac{i^0 N}{\pi^{1/2}} \int_0^t \frac{i(u)}{(t-u)^{1/2}} du - \nu C_d - \frac{2i^0 N}{\pi^{1/2}} \nu C_d \sqrt{t} - \frac{Fi^0}{RT} vt \quad (20)$$

Finally, the equation of linear voltammetry of potential for low overvoltages and times is obtained, in the two cases:

- if the capacitive current is neglected:

$$i(t) = -\frac{Fi^0}{RT} vt \left(1 - \frac{4i^0 N}{3\pi^{1/2}} t^{1/2} \right) \quad (21)$$

- if the capacitive current is taken into account:

$$i(t) = -\frac{Fi^0}{RT} vt \left(1 - \frac{4i^0 N}{3\pi^{1/2}} t^{1/2} \right) - \nu C_d \quad (22)$$

The obtained equations facilitate the determination of the standard density of the exchange current and the specific capacitance of the electrochemical double layer.

Basic Faraday Impedance Method

In the case of inert metal/redox electrolyte electrodes, a very low overvoltage is applied to the steady-state interface, analyzing the current density passing through the faradic impedance (Z_F) of the interface. Depending on the nature of the electrode redox reaction, a phase difference occurs between the overvoltage and the current density.

If this is irreversible, the limitations are by charge transfer, Z_F is given only by the charge transfer resistance (R_{ts}), and the two parameters are in phase ($\varphi = 0$).

If the reaction is reversible, the limitations are by mass transfer, namely diffusion, Warburg impedance, Z_W , is given by the two components R_W and C_W , and the two parameters are phase shifted with φ .

In the case of quasi-reversible reactions, all three elements (R_{ts} , R_W , C_W) occur, and the phase shift value φ is based on their relative contribution. In this case, the Fredholm equation becomes:

$$i_F = I_F \sin \omega t = \lambda \frac{i^0 N}{\pi^{1/2}} \int_0^t \frac{I_F \sin \omega(t-u)}{u^{1/2}} du - \frac{Fi^0}{RT} \eta(t) \quad (23)$$

The basic Faraday impedance method determines the dependence of R_s and C_W on the frequency/pulse of the alternating current.

2.2. Experimental Method/Model

Molecular machines with electro-photo-chemical activation

In the case of pseudorotaxane, as shown in Figure 4 (top), their formation is favored by non-covalent interactions between the ring and the axis, which can be modulated by an external stimulus, thus controlling threading and dethreading [7-9] of molecular components. In the case of rotaxanes, two main movements with high amplitude can be made: translation by ring movement along the axis (Figure 4 – middle); rotation – by the ring movement around the axis (Figure 4 – bottom). Consequently, rotaxanes are prototypes suitable for the construction of both linear and rotary molecular machines. Indeed, systems of the first type, called molecular shuttles [10], are the most common implementation of the rotaxanes in the concept of molecular machines.

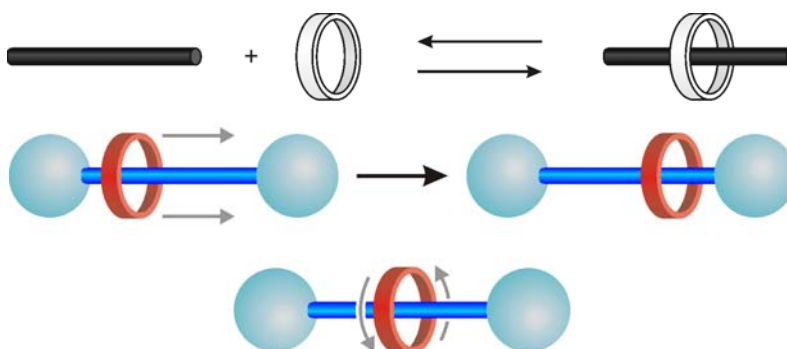


Figure 4. TOP: Schematic representation of the threading-dethreading equilibrium in the case of pseudo-rotaxanes, involving the axle and ring components [7-9]; MIDDLE: Schematic representation of the translational movement of the ring in the case of rotaxanes; BOTTOM: Schematic representation of the rotation of the ring in rotaxanes [10]

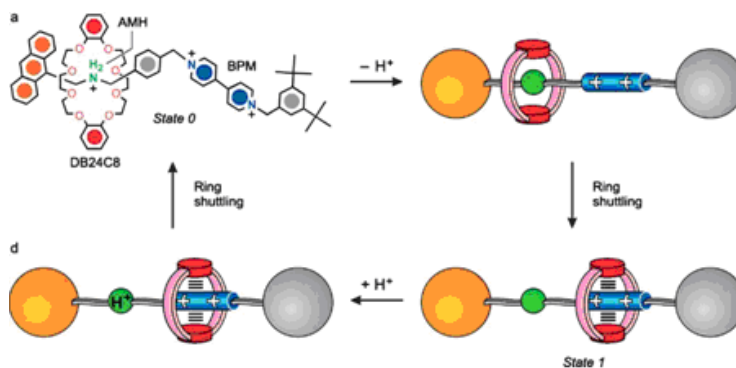


Figure 5. Chemical structure and operation of an acid-base controllable rotaxane (Ashton et al. 1998) [11]

An example of molecular machines that behaves as a reversible molecular shuttle is controlled by acid-base stimulation (Figure 5) [11]. It is made up of an axial component containing an ammonium ion (AMH) and an electron acceptor bipyridine unit which can

establish hydrogen bonds and charge transfer interactions with the ring component that is a dibenzo [24-]-8 crown ether. An anthracene group is used as a stopper because its absorption, luminescence and its redox properties are useful to monitor the status of the system.

As long as the interactions of the hydrogen bond $N^+ \cdots H \cdots O$ between the macrocyclic ring and the ammonium center are much stronger than the charge transfer interactions of the ring with the bipyridine unit, rotaxane exists only as one of the two possible translational isomers (Figure 5.a, state 0). Deprotonation of the ammonium center with a base (Figure 5.b) determines the displacement of the ring in percent of 100% by Brownian motion to the bipyridine unit (Figure 5.c, state 1); reprotonating rotaxane with an acid (Figure 5.d) directs the ring back to the ammonium center.

3. PERSPECTIVES

3.1. Rotaxane with integrated and photo-activated redox mechanism. Shuttle processes for rotaxanes

As previously mentioned, the rotaxane's common implementation in case of molecular machines is the development of molecular shuttles in which translational movements of the ring occur [12,13]. This type of molecular machines must have a well-organized structure and should work as multicomponent systems with proper functional integration [14,15].

Usually, rotaxanes are made of an axle-shaped component, equipped with two distinct recognition centers – the stations, and a ring that performs the shuttle movement between the two stations. Initially, the ring is placed on the station that is a better recognition center for it; in the case of suitably designed rotaxanes, the shuttle movement to the other station may be induced by light-powered electron transfer processes [8,16,17]. In this case, the photoinduced shuttle movement may occur, which involves the following main steps:

1. *Destabilization of the stable translational isomer*: the light excitation of the photoactive unit is followed by an electron transfer from the excited state of this unit to the ring-surrounded station, with the consequence of station deactivating;
2. *Ring movement*: the ring moves from the reduced station to the other one;
3. *Electronic Reset*: the reverse transfer of the electron from the reduced “free” station takes place to the photoactive unit, which gives the power of the electron-acceptor to this station;
4. *Nuclear Reset*: The ring moves back to the preferred station with the consecutive restoring of the structure from the beginning.

The critical points of this mechanism [8,16,18] are the competition between the photoinduction process of electron transfer and the deactivation of the intrinsically excited state, and between the shift of the ring at the reduced station and the reverse electronic transfer process. However, if the system is properly designed and optimized, each absorbed photon facilitates a forward and backward movement of the ring between the two stations, making a complete mechanical circuit.

Thus, rotaxanes of this type act as a four-stroke autonomous motor [17,18], where the visible light represents the fuel and the intramolecular processes correspond to the following stages: 1) fuel injection and combustion (destabilization of the initial structure); 2) displacement of the piston (displacement of the ring); 3) Exhaust gas evacuation (electronic

reset); 4) piston displacement (nuclear reset). Note that the photoinduced shuttle process of the ring can also occur with an external electronic relay.

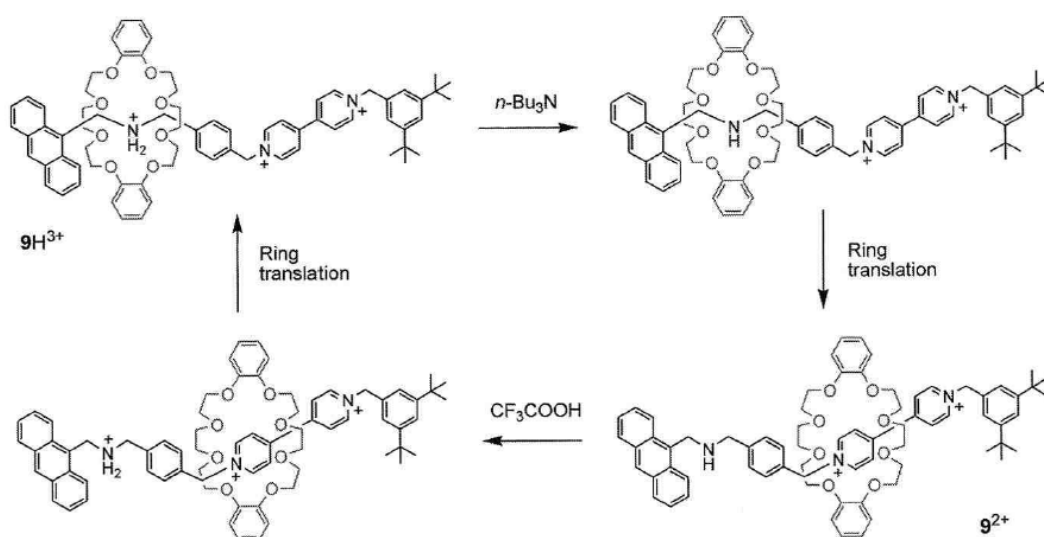


Figure 6. The formula of rotaxane $9H^{3+}$ structure and the representation of its functioning as a pH-controllable molecular shuttle

All the new devices and machines which can perform useful light-induced functions are of the highest importance nowadays [19].

In this context, the paper stage is in the quantum-computational modeling phase, from the perspective of the chemical reactivity, chemical electroreactivity for the complex rotaxane molecular machine presented in Figure 6. The electrochemistry of the $9H^{3+}$ [2]rotaxane is closely related to its structure, namely:

- a dibenzo[24]crown-8 ether (DB24C8) – π electron donor macrocycle;
- a dumbbell component containing a secondary ammonium center ($-NH_2^+$) and a 4,4'-bipyridine unit (bpy^{2+});
- as stoppers: a functional group of anthracene at one end, and a 3,5-di-tert-butylphenyl group at the other end,

and also, besides the *in silico* – *in vitro* complete characterization, aims its subsequent functionalization in the graphene matrix, with the perspective of replacing moletronics with molecular circuits integrated on graphene, in graphenetric engineering of carbon microcircuits with a molecular capacitor.

3.2. Chemical Electro-Reactivity with Molecular Machines. From moletronics to inclusive graphenetric

As in the case of electrons, photons play a double role [8,20], namely: they supply the energy required by the system and have the ability to highlight changes induced in the system – which means that photons can also be used to write and read the status of the system [21].

The photoinduced energy and electron transfer reactions can be exploited to connect light-supplied energy with the mechanical, electrical and optical functions of molecular devices and machines [17,21]. These processes represent the basis of the bottom-up construction of light-powered nanoscale devices and machines [22].

Thus, the general acid-base processes are transposed at the electrochemical level by photoactivation of the molecular machines, by the following process sequences occurring in a supramolecular system A-L-B type [7,22], where:

- A is the molecular unit that absorbs light;
- B is another molecular unit involved in light-supplied processes;
- L is the connection unit (also known as “bridge”).

Under the influence of excitation light, the photoexcitation process takes place according to the equation:



In this case, the two partner reactions are already of convenient duration and may undergo the transfer of electrons in the variants:



In the absence of further processes (such as decomposition of oxidized or reduced species), photoinduced electron transfer processes are followed by spontaneous reverse electron transfer reactions that regenerate the initial state of the system:



and the photoinduced energy transfer is followed by the radiation or non-radiation deactivation of the excited acceptor:



In supramolecular systems, electron and energy transfer processes can often involve exciting states with very short lifetimes.

The current challenge resides in the identification of functionalized graphene devices with photo-activated molecular machines based on the sequences of the processes as mentioned above, and their proper selection, respective deca-nano-graphenic integration. It is not to be ignored the possibility of controlling photoisomerization, as another interesting light-induced process that can be exploited for the operation of molecular devices and machines [8,16,22].

4. DISCUSSION AND CONCLUSION

Generally, photo-electrochemical observables are monitored for the graphene nano-deca-semiconductor functionalized with molecular machines to control the Coulomb blockade (Figure 7), with various graphene integration phases observed by atomic force microscopy.

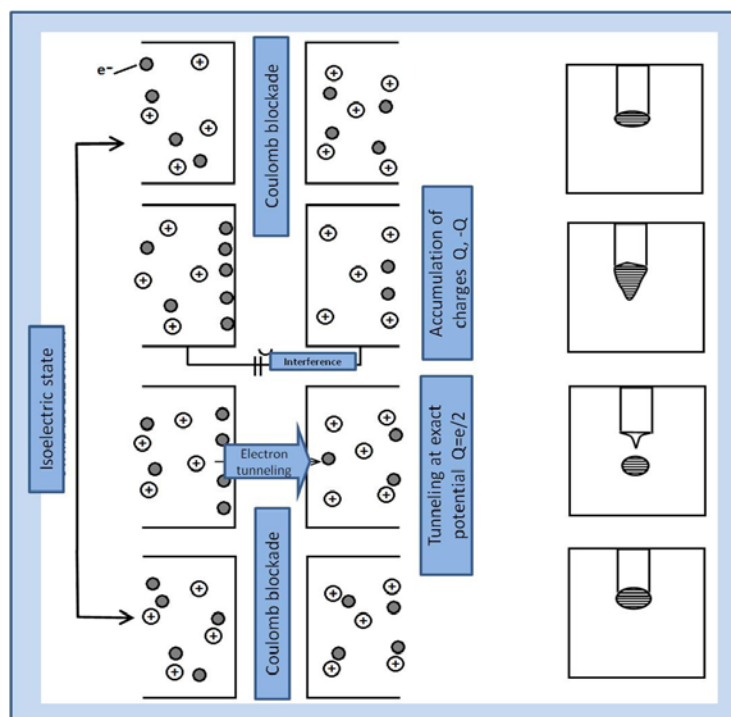


Figure 7. Nano-electro-scopic phenomenology of the Coulomb blockade (left), and its macroscopic correspondence (right)

In the present case, the phenomenon of the Coulomb barrier involves three correlated aspects, namely:

- the occurrence of a band gap (BI) around the Fermi level in the energy spectrum of electrons limited in semiconductor quantum dots or in small metallic particles (generically speaking, in islands) that are coupled to metallic wires by tunneling barriers;
- BI – the additional energy required due to the Coulomb interaction between the electrons of the island, for an electron to tunnel into or from the island;
- tunneling/redistribution of electrical charge – expressed by a change in the electrostatic potential.

Once optimized, the Coulomb blockade allows precise control of a small number of electrons with essential applications in switching devices with low power dissipation and thus an increase in the circuit integration level.

For the next step – the functionalization of graphene matrices with molecular machines, the successive actions are:

- the structures of molecular machines (rotaxanes/catenanes) considered more important are represented in Hyperchem [23];
- the chemical reactivity, transfer energy and other parameters that can be obtained based on the HSAB are calculated;
- for the studied systems, the Coulomb blockade is estimated;
- predictions are made on the photovoltaic effect bondonic type, using bondonic spectral relations;

- the thermodynamic indices of interconversion (free energy, enthalpy, entropy, etc.) in the case of molecular machines, are calculated through the path integral formalism;
- by the similarity between molecular machines and binary logic systems (Figure 8) the logical amount of information is provided, estimating the type of logic system (AND, OR, XOR, etc.) corresponding to the state of the molecular machine during operation.

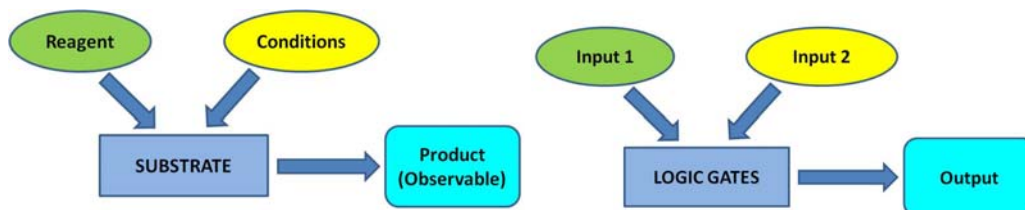


Figure 8. The schematic representation of the similarity between a chemical process (left) and a logical system (right)

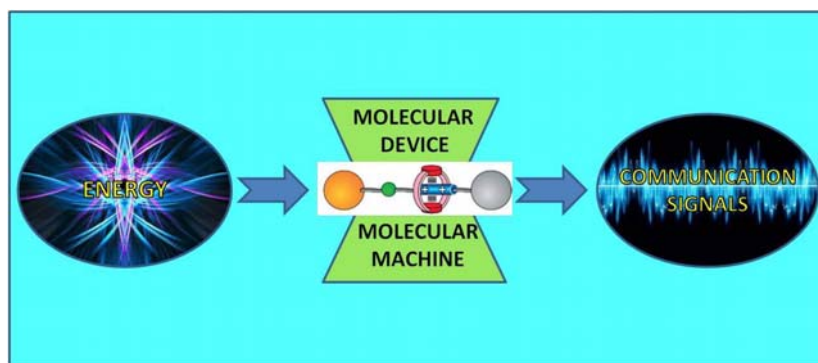


Figure 9. Sustainable transfer from energy to information with the aim of molecular machines integrated into devices, molecular and graphenetric

Finally, the molecular machines – by functionalizing the quantum deca-nano-quantum semiconductor, which is integrated as an electronically activated microcircuit, provide electro-logical, controlled, activated, intelligent and sustainable functions (Figure 9), as follows:

- represents switches at which the output (0 or 1) depends on the input (0 or 1);
- can generate the AND logic gate – the logic product between the inputs, the output signal is 1, all the inputs are 1; the equivalent circuit consists of switches in series;
- can generate OR logic gate – the logic sum between inputs, the output signal is 1, if at least 1 of the inputs has the value 1; the equivalent circuit consists of switches in parallel;
- can generate the XOR (eXclusive OR) logic gate – more complicated than the AND and OR logic gates, and the logic circuit contains two bipolar switches; output – as in the case of OR logic gate but is 0 if both inputs are 1; basically, this is a comparator that can determine whether two inputs have the same value;
- ensures the development of molecular systems that act as logic circuits;
- represent systems that convert the input stimulus (optical, electrical or chemical) = input into output signals (which may also be of optical, electrical or chemical nature) = output.

ACKNOWLEDGEMENT

We hereby acknowledge the research project PED123/2017 of UEFISCDI-Romania.

REFERENCES

1. Reed, M.A. Molecular-scale electronics, *Proceedings of the IEEE* **1999**, *87*, 652-658.
2. Venturi, M.; Balzani, V.; Ballardini, R.; Credi, A.; Gandolfi, M.T. Towards molecular photochemionics, *Int. J. Photoenergy* **2004**, *6*, 1-10.
3. Bockris J.O'M., Khan, S.U.M. *Quantum Electrochemistry*, Plenum Press, New York, USA, **1979**.
4. Bieniasz, L.K. *Modelling Electroanalytical Experiments by the Integral Equation Method*, Springer Verlag Berlin, **2015**.
5. Bonciocat, N. *Electrochimie și aplicații*, Ed. Dacia Europa-Nova, Timișoara, România, **1996**.
6. Bonciocat, N. *Alternativa Fredholm în Electrochimie*, Ed. Mediamira, Cluj-Napoca, România, **2005**.
7. Balzani, V.; Credi, A.; Venturi, M. *Molecular Devices and Machines. Concepts and Perspectives for the Nanoworld*, Wiley-VCH, Weinheim, **2008a**.
8. Balzani, V.; Credi, A.; Venturi, M. Light powered molecular machines, *Chem. Soc. Rev.* **2009**, *38*, 1542-1550.
9. Ragazzon, G.; Baroncini, M.; Silvi, S.; Venturi, M.; Credi, A. Light-powered, artificial molecular pumps: a minimalistic approach, *Beilstein J. Nanotechnol.* **2015a**, *6*, 2096-2104.
10. Balzani, V.; Bergamini, G.; Ceroni, P.; Vogtle, F. Electronic spectroscopy of metal complexes with dendritic ligands, *Coord. Chem. Rev.* **2007**, *251*, 525-535.
11. Ashton, P.R.; Ballardini, R.; Balzani, V.; Baxter, I.; Credi, A.; Fyfe, M.C.T.; Gandolfi, M.T.; Gómez-López, M.; Martínez-Díaz, M.-V.; Piersanti, A.; Spencer, N.; Stoddart, J.F.; Venturi, M.; White, A.J.P.; Williams, D.J. Acid-base controllable molecular shuttles, *J. Am. Chem. Soc.* **1998**, *120*, 11932-11942.
12. Bissell, A.; Cordova, E.; Kaifer, A.E.; Stoddart, J.F. A chemically and electrochemically switchable molecular shuttle, *Nature* **1994**, *369*, 133-137.
13. Arduini, A.; Bussolati, R.; Credi, A.; Pochini, A.; Secchi, A.; Silvi, S.; Venturi, M. Rotaxanes with a calix[6]arene wheel and axles of different length. Synthesis, characterization, and photophysical and electrochemical properties, *Tetrahedron* **2008**, *64*, 8279-8286.
14. Balzani, V.; Credi, A.; Venturi, M. Molecular machines working on surfaces and at interfaces, *Chem. Soc. Rev.* **2008b**, *9*, 202-220.
15. Balzani, V.; Bergamini, G.; Ceroni, P. From the photochemistry of coordination compounds to light-powered nanoscale devices and machines, *Coord. Chem. Rev.* **2008c**, *252*, 2456-2469.
16. Credi, A.; Venturi, M. Molecular machines operated by light, *Cent. Eur. J. Chem.* **2008**, *6*, 325-339.
17. Balzani, V.; Bergamini, G.; Marchioni, F.; Ceroni, P. Ru(II)-bipyridine complexes in supramolecular systems, devices and machines, *Coord. Chem. Rev.* **2006a**, *250*, 1254-1266.

18. Balzani, V.; Credi, A.; Venturi, M. Controlled disassembling of self-assembling systems: Toward artificial molecular-level devices and machines, *Proc. Natl. Acad. Sci. USA* **2006b**, *99*, 4814-4817.
19. Venturi, M.; Iorga, M.I.; Putz, M.V., Molecular Devices and Machines: Hybrid Organic-Inorganic Structures, *Current Organic Chemistry* **2017**, *21*, 27, p.2731-2759.
20. Balzani, V.; Bergamini, G.; Ceroni, P. Light: a very peculiar reactant and product, *Angew. Chem. Int. Ed.* **2015**, *54*, 11320-11337.
21. Ceroni, P.; Credi, A.; Venturi, M. Light to investigate (read) and operate (write) molecular devices and machines, *Chem. Soc. Rev.* **2014**, *43*, 4068-4083.
22. Balzani, V., Ceroni, P., Juris, A. *Photochemistry and Photophysics. Concepts, Research, Applications*, Wiley-VCH, Weinheim, **2014**.
23. Iorga, M.I.; Putz, M.V., Application of Molecular Machines in Photoelectrochemistry, In *Proceedings of The 24th International Symposium on Analytical and Environmental Problems*, University of Szeged, Hungary, 8-9 October 2018, Alapi T., Ilisz I., Eds., Published by University of Szeged, **2018**, pp.363-367.

Research Review

ELECTROCHEMICAL SYSTEMS AND MECHANICALLY INTERLOCKED MOLECULES. PART 2: NANO-TECHNOLOGY

Mirela I. Iorga (1,2), Paula Svera (1), Doru Buzatu (1), and Mihai V. Putz (1,2, *)

1. Laboratory of Renewable Energies-Photovoltaics, R&D National Institute for Electrochemistry and Condensed Matter –INCEMC–Timisoara, Timisoara, Romania
2. Laboratory of Structural and Computational Physical-Chemistry for Nanosciences and QSAR, Biology-Chemistry Department, West University of Timisoara, Timisoara, Romania

ABSTRACT

Due to the difficulties encountered by moletronics in the realization of viable microcircuits based on microconductive bridges and nanoelectrodes, the current research aims to produce controlled deposited graphene microcircuits, in the form of lamellar multilayer, quantum coupled and functionalized with molecular machines, matrix configurations, which is an innovative approach compared to the present transversal heterojunction. From this assembled system, the resulted quantum clusters can stock the molecular energy using local effects, specific for spin quantum electrochemistry, and by photo-activation of integrated micro-circuit with logic gates in the form of deposited quantum graphene clusters, potential and quantum efficiency was investigated.

Keywords: spin quantum electrochemistry, graphene, molecular machines, graphenetrionics, logic gates

1. INTRODUCTION

Starting with the Nobel Prize for Graphene, latest studies regarding graphene materials are established on creative, innovative, disruptive dynamic technology [1]. These are directed on developing original producing methods [2-4], including nano-system topology, through the fundamental quantum mechanism of generating Stone-Wales defects on graphene [5], an essential effect both in the phenomena of magnetization to which graphene can participate, but also in its superconducting deca-nano-conductive functions [6].

According to the “Lemma of New Technology” stated by Herbert Kroemer, awarded in 2000 with the Nobel Prize in Physics for Pioneering Work in Information Technology and

Communication, it seems that “applications of any sufficiently new and innovative technology always have been – and will continue to be – applications created by that technology”. This postulate could be applied to the later discovery of graphene as a new state of matter (Nobel Prize in Physics 2010 awarded to Andre Geim and Konstantin Novoselov “for groundbreaking experiments regarding the two-dimensional material graphene”). From this point of view, graphene is still considered a rising star in the science of materials, with a strictly bi-dimensional nature (2D) and particularly efficient power and heat conduction ability. Consequently, graphene no longer requires further evidence of its importance in terms of physical fundamentals, because it “is probably the only system where ideas from quantum field theory can lead to patentable innovations“ – as Frank Wilczek said (awarded with Nobel Prize in Physics in 2004 for “the discovery of asymptotic freedom in the theory of the strong interaction”). From this point starts the possibility for the creation of smart material applications with nano-ecological energy functions in photovoltaic systems, with the aim to enhance the conversion of the sunlight energy into green electricity, based on its properties and a thin structure composed from a single layer of carbon atoms. Besides this remarkable ability, graphene structure could also be outstanding support for the concept of quantum-particle wave function/chemical bond field, bondon, in chemical bond field modeling. In its turn, is a boson, bondon can be associated in clusters, delocalized quantum dots, called bondots (bonding of quantum dots) – particles that describe the coherent links of quantum points occurring in condensed matter, including graphene. Since quantum dots (QD) have already proven their usefulness for solar cells through their sensitization potential, the present multi/matrices (bondotic) quantum dot – MQD approach, can generate a new production of amplification of light, this time at the photovoltaic level, promoting a new generation of solar cells of energy materials working on such a mechanism.

The Graphene study is very advanced in developed economies, based on a creative, innovative, disruptive dynamic technology. There is a comprehensive review in 2015 – with a projection for 2030 of graphene science and technology pioneers, including Nobel Prize winners for Graphene [1]. Also, there is the author’s series with the reputed Prof. Franco Cataldo, one of Italy’s few leading contractor manufacturers of graphene, developing an original method of producing fullerene base graphene [2-4]. Also, there is the author’s series with Dr. Ottorino Ori, a pioneer in the fullerene nano-systems topology, by the significant article on the quantum mechanism of generating Stone-Wales defects on graphene [5]. They are essential both in the magnetization phenomena to which graphene can participate, but also for its function conductive, superconducting [6], semiconductor, hole (h) or electron (e) deca-nano-systems, the base for the graphene quantum transistor.

Instead, molecular machines, rotaxanes, and catenanes have been designed and synthesized as dynamic systems stabilized by non-covalent bonds/interactions between components that contain complementary recognition centers [7-14]. In particular, rotaxanes are prototypes suitable to the construction of linear and rotational molecular machines, with the typical development of molecular shuttles allowing translational movements of rotating rings [15,16]. These types of molecular machines are dynamic, stable structures with functional integration capability in multicomponent systems [17,18], so also on/with graphene (even if this system is not yet studied). However, self-electrochemistry of molecular machines opens opportunities for what can be called (quantum) logic gates; thus, Credi et al. [19] proposed a structure of a pseudorotaxane formed in solution by the self-assembling of the 2,7-dibenzylidiazapyrene dication (as a wire type electron acceptor) and 2,3-dinaphtho-30-crown-10 (as an electron donor macrocycle). The compound may be unthreaded or rethreaded by chemical inputs, for example, the unthreaded process involves the addition of stoichiometric amounts of acids or amines, while the amine addition can achieve rethreaded, and vice versa. These threading/unthreading processes can be monitored taking into account

the essential changes in the fluorescence properties of the system. By two sets of different species with common and specific traits, two distinct and reversible unthreading/rethreading cycles can be achieved. The system can be considered as an XOR logic gate because of the system characteristics: input – chemical and output – fluorescence.

In Romania, studies about and with graphene, including its production in the laboratory, are becoming more common (including INCEMC-Timisoara) [20], but especially for its applications based on high electrical and thermal conductivity. In contrast, in terms of molecular machines, we have no knowledge of Romanian groups and researches – apart from those published by some of the authors of this paper – co-authors with Professor Margherita Venturi [21] (recognized co-worker of Nobel laureate for molecular machines, Sir J. Fraser Stoddart [22]) with the best intention to identify and collaborate with the active and potential national partners.

The present paper, advances the combined graphene + molecular machine system with the applicative research of photo-energy generated and stored by the resulting deca-nano-system, by electro-quantum spin activation, as follows.

2. METHODS AND MODELS

From this point, the present paper proposes the systematic study of graphenetrionics through innovative, theoretical and experimental methods, with a high potential to create a new solar cell prototype (based on the quantum deca-nano-transistor/semiconductor). Also the paper advance the graphene-integrated circuits, functionalized with photoactivated, spin-coupled molecular machines, arranged as a matrix in a controlled manner, which facilitates redox phenomena by quantum tunneling (spin quantum electrochemistry).

The proposed research is divided into the following stages regarding the design, testing and calibration of nano-systems with graphene with photoelectric energy conversion function and their storage in molecular machines/motors:

1. **Graphenetrionic Engineering** (concerning *Electronic algebra on Graphene*, and *Graphenic Matrix Heterojunctions*) aimed to guide the modeling and experimental observation of the “green” over-current (on graphene support) with the help of graphenetrionics, through innovative matrix heterojunction configurations.
2. **Molecular Machines with Photoactivated Graphene** (concerning *The second kind Storage of Energy for Molecular Machines with Graphene*, and *Electrochemical Reactivity with Spin Molecular Machines*) regarding the storage of the molecular current (over-micro-current) with molecular machines (Figure 1) functionalized on graphene support.
3. **Graphene Quantum Electrochemistry** (concerning *Nano-Imaging Control of Quantum Tunneling on Multilayer Graphene*, and *Electrochemical Quantum Metrology*) controlling the electrochemical flow with defective graphene in quantum logic gates configurations.
4. **Spin Density Photoactivation on Semiconducting Graphene** (concerning *Activation of Quantum Logic Gates on Defective Graphene*, and *Superconductivity of Magnetized Deca-Nano Graphene Semiconductor*) controlling the electrochemical photo-current with the aid of defective and spin coupled (magnetized) graphene in matrix configurations such as quantum logic gates.

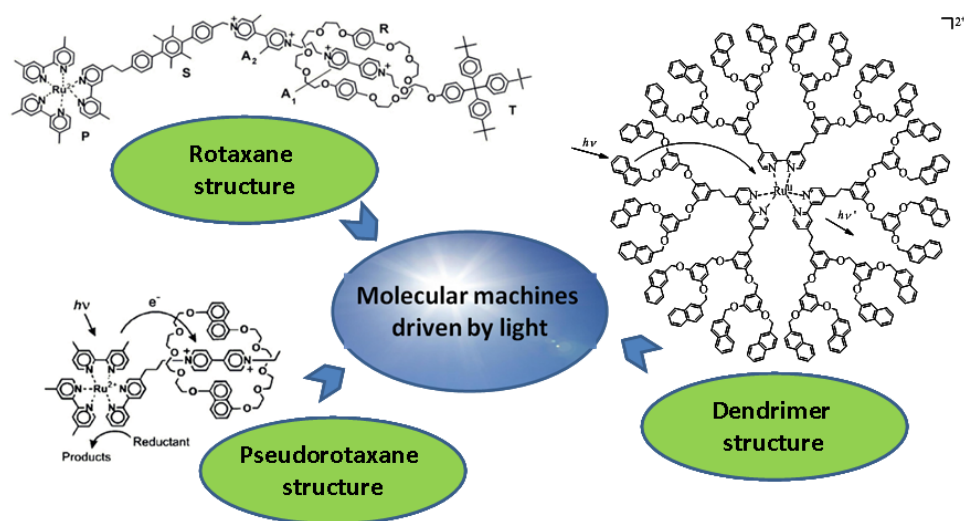


Figure 1. Fundamental types of molecular machines, self-electrochemical structures under the action of light [23]

Regarding all the previously described statements, this research also contributes significantly to the present and future sustainability of Econo-ecological nano-energy efficiency as follows:

- ✓ Scientifically – by advancing a mechanism (graphene + molecular machines + bondonic and bondotic photoactivation) of energy generation and storage at the nanoscopic level (smart bottom-up approach);
- ✓ Technologically – by advancing a prototype of photovoltaic energy storage on graphene functionalized with molecular machines, respectively replacing silicon-based integrated circuits with other technologies based on graphene functionalized with molecular motor capacitors, that exhibit magnetic response, with a spin coupling on matrix depositions (the effective top-down approach);
- ✓ Socio-economic – by creating and storing green, non-toxic, carbon-based (graphene) energy with electrochemical control and autonomy (viz. molecular machines), with the perspective of technological transfer and leap from the scientific-technological disruption to innovation of devices and accessories (including household, but also medical, educational, info-communication, encryption and cyber-security) based on solar cells and photoactivated integrated circuits (sustainable multi-stakeholder approach).

2.1. Conceptual Approach

Graphene has already entered in the leading scientific flow as a support for both fundamental research (band structure, heterojunctions) and applicative research (photovoltaic, electrochemical effects, graphene environment both as an electrode and sensitization medium, replacing, at least from a non-toxic perspective, the generation of solar cells based on organic sensitizers and dyes). On the other hand, molecular machines, although very recently recognized as producing the smallest autonomous systems at the molecular, nanoscopic level, are barely at the stage of synthesis and observation; however, they can control the auto-oxidation-reduction mechanism under the influence of light. Including both, graphene and molecular

machines, the present research highlights two significant debuts. First of all is the functionalization of molecular machines supported on graphene, as a premise of a combined deca-nano-system that can generate (by graphene) + storage (by molecular machines) photo-energy produced by light activation or spin coupling (magnetization), or by both conjugated mechanisms (simultaneous or stepwise). The other is the phenomenological combination in various systems acting as quantum logic gates (on/off by electronic tunneling at mono-atom or mono-ion level charge carrier from the system). Graphene functionalized with Molecular Machines Integrated Circuits (acting as molecular capacitors, based on self-electrochemical processes) in matrix-designed configurations will substitute the Silicon Integrated Circuit Technology. Also, they will replace the bi- and multi-graphenic cross heterojunctions (staging type), attributed to the van der Waals interaction and hence Coulomb blockade, acting as electronic transfer speed limiters.

As a result, it can define (and possibly impose, through this research), the new electronic approach (including integrated circuits) with graphene belongs to GRAPHENETRONICS, and by functionalization with molecular machines and matrix combinations with them, having an electronic control mean – SPIN QUANTUM ELECTROCHEMISTRY.

2.2. Experimental Idea of Graphenetrionic Engineering. *Electronic Algebra on Graphene*

The deposition of the selected materials (such as graphene oxide systems GO and TiO₂) was carried out by drop casting (Figure 2) as follows:

- Several dripping methods were tested to obtain the smallest deposition diameter (using, for example, needle, pen, and micropipette). All preliminary tests were applied on the glass, and only the most regular shaped depositions were optimized.
- The second step consisted in depositing GO and TiO₂ on ITO as presented in the Figure 2.
- The diameter and distances between the droplets were determined using the microscope (Olympus BX51 halogen lighting system – 100W, focusing capability of 0.1 mm = focus sensitivity with Nikon LU Plan Fluor 10x/0.30 A, OFN25 WD 17.5 lens).
- Next step, alternative graphene/oxide configurations will be realized, aiming to create a matrix of periodical deposits, bi- or multi-component, to replace cross heterojunctions. These will be further studied, concerning quantum contacts, short circuit, open circuit, and photo-activation, with selection and comparison of response signals.

The unique/distinct responses in the electro-/photo-current recorded on the matrix plates will be associated with nano-energetic conversion matrices, precursors of the graphene integrated circuits.

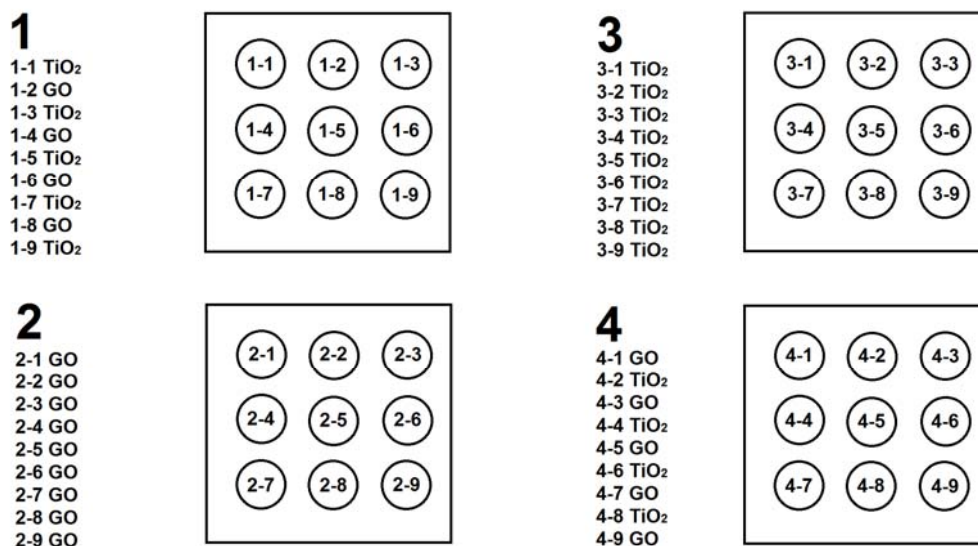


Figure 2. Matrix positions of GO / TiO₂ depositions on ITO glass

3. FIRST RESULTS AND DISCUSSIONS

Determination of coefficients by measurement, comparison, interpolation, metrological calibration (with Hall, Josephson, and tunneling quantum effects) combines the algorithm for each matrix multi-graphene deposition and provides the basis for the projection and realization of the quantum transistor with photo-activated graphene.

3.1. Graphenetric Engineering. *Graphene Matrix Heterojunctions*

Transforming the response of electro-voltaic matrices for the graphene/oxide deposits from the previous phase into the quantum matrices associated with the applied potential $V(x, y, z)$, through the densities of generated states $\rho_n(x, y, z)$, to a given (or varied) thermal energy according to Boltzmann's relationship $\beta = 1/Tk_B$, with the observation of the current density provided by the Eq.(1):

$$j_n[V(x, y, z)] = (\eta\beta V(x, y, z))^{-1} \iiint \rho_n(x, y, z) V(x, y, z) dx dy dz \quad (1)$$

The quantum supercurrent identified corresponds to the critical temperature for which the electronic fermion spin (fermion electron) $\rho_{Fermi-Dirac}(x, y, z)$ passes into the bosonic states of the bondons $\rho_{Bosonic-Bondon}(x, y, z)$, with the identification of the respective boson accumulation by clusters identified in Atomic Force Microscopy (Figure 3) for different graphene structures (and origins).



Figure 3. Phase transition on combined fullerene graphene systems through the AFM technique. (a) Left - Graphene oxide dissolved in water – “Graphenea” in an isopropyl alcohol solution. (b) Center - Graphene oxide dissolved in water – “Graphenea” in ethylene glycol solution. (c) Right - Graphene oxide dissolved in water – “Graphenea” in water

3.2. Molecular Machines with Photoactivated Graphene. *The second kind Storage of Energy for Molecular Machines with Graphene*

It is considered as a working system a rotaxane-based molecular machine, in fact [2]rotaxane $1H^{3+}$ containing a π electron donor macrocycle, dibenzo[24]crown-8 ether (DB24C8), along with a “dumbbell” component consisting of a secondary ammonium ($-NH_2^+$) and a 4,4'-bipyridine unit (bpy^{2+}); the stopping system consists of an anthracene unit on one side and the 3,5-di-tert-butylphenyl group on the other side. The system is stable to charge transfer (CT) due to the weak interaction of the electron-p donor macrocycle with the bpy^{2+} p-electron acceptor unit, compared to the interaction of the hydrogen bond [$N^+-H \cdots O$] between the DB24C8 macrocycle and the ammonium center, when the macrocycle surrounds the center (Figure 4).

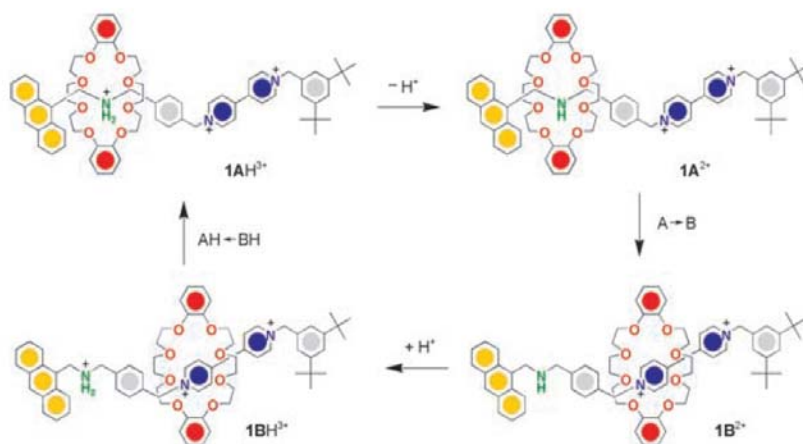


Figure 4. Schematic representation of a molecular shuttle process of a rotor-crown ether by deprotonation and reprotonation of the ammonium center [13]

However, if a base such as tributyl amine is added, the ammonium center is converted to an amine function with a $1A^{2+}$ transition state, and after the macrocycle dislocation in the bpy^{2+} unit is switched to the stable $1B^{2+}$ state. The process is reversible if an acid, such as trifluoroacetic acid, is added when the system returns to its original state by the $1BH^{3+}$

transition state. If the rotaxane is deprotonated, for example by uni-electronically reducing of the bipyridine unit, the charge transfer channel is destroyed, and the macrocycle ring can be detached from the bpy^{2+} station. This step consists of calibrating a self-electrochemical process with molecular machines, testing and measuring of the thermodynamic functions (free enthalpy, formation enthalpy, and Gibbs energy) for the case where the process is carried out on graphene at locations selected from the matrix deposits in the earlier stages of the research.

3.3. Molecular Machines with Photoactivated Graphene. *Electrochemical Reactivity with Spin Molecular Machines*

The spin chemical reactivity is modeled in the auto-electrochemical system from the previous stage for estimating the storage energy (at each such internal electrochemical cycle) following the energies released by electronic destabilization and restoration, in an isolated state (Figure 5) – respectively on graphene support.

As an acid-base process, the “Hard and Soft Acids and Bases” (HSAB) principle in the Parr-Pearson variant is applied, whereby the energy transferred/stored in an acid-base transformation cycle, the induced electrochemical phenomenon is written in an additive way (see quantum superposition principle):

$$\Delta E = \Delta\Omega_A + \Delta\Omega_B \quad (2)$$

but with mixed contributions (see quantum interference) of the type:

$$\Delta\Omega_A = -\frac{\eta_A}{4(\eta_A + \eta_B)^2} (\Delta\chi)^2 \quad (3)$$

$$\Delta\Omega_B = -\frac{\eta_B}{4(\eta_A + \eta_B)^2} (\Delta\chi)^2 \quad (4)$$

with the determinant as the difference in electronegativity of the reactants:

$$\Delta\chi = \chi_A - \chi_B \quad (5)$$

The optimal energy condition (storage) implies, for example, the minimization of the contribution $\Delta\Omega_A$ concerning the chemical strength η_A , while the electronegativity variation $\Delta\chi$ and the chemical strength of the counterpart η_B are kept constant (stabilized).

It should be noted that the HSAB principle implies the optimal transfer (excess energy storage, possibly via functionalization with the graphene support) until the HOMO-LUMO differences for the electrochemically reactive species are equilibrated $\eta_A = \eta_B$, respectively coordinate weak acids with weak bases and strong acids with strong bases.

The computational modeling in HyperChem [24], as in Figure 5, allows the obtaining of a complete energy panel (HOMO and LUMO spectral calculation) to optimize inter-band energy couplings to the cycle functionalization of the molecular machines with the graphene structure matrix deposited as above.

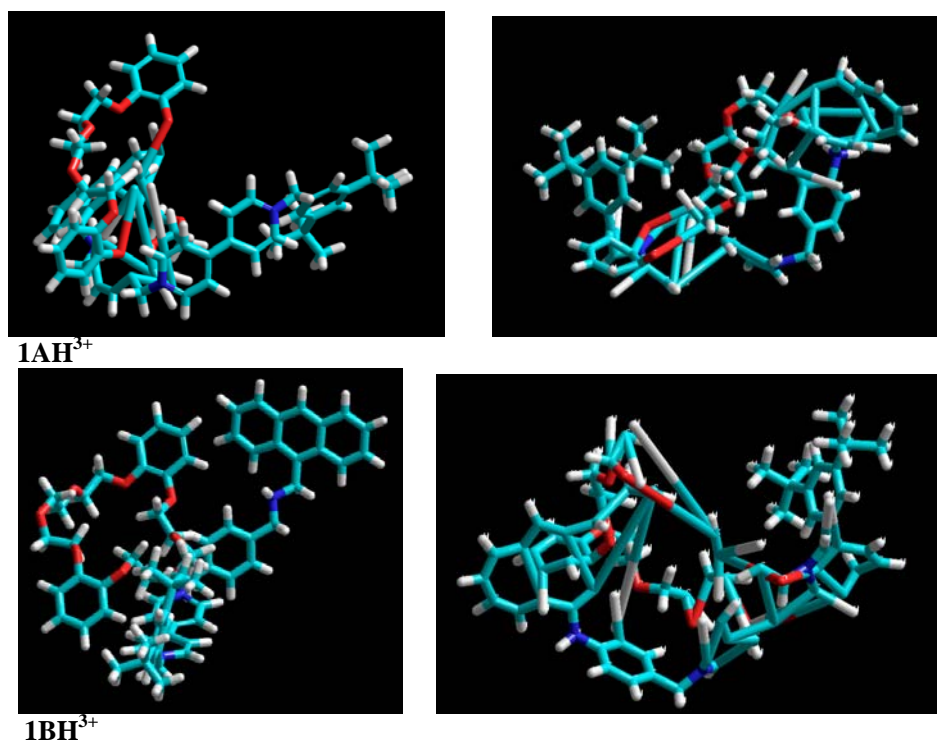


Figure 5. HyperChem representations [24] of molecular shuttle structures and internal electrochemistry from Figure 4

3. 4 Graphene Quantum Electrochemistry. *Nanoscience Control of Quantum Tunneling in Multi-Graphene Systems*

In the multigraphene context, as the result of electronic coupling, bondonic forms occur in three structural forms. First of all is the chemical-graph $|0\rangle$ corresponding to the isolated state, then the state of a grid/node (in Figure 2) as vacation type or defective hole $|h\rangle$, respectively the pre-bosonic topological/electronic defective state $|e\rangle$, corresponding to the “quantum sea” which incorporates the space of the topological isomers in the multigraphenic matrix node. Given that these states can simultaneously exist in a multigraphene matrix arrangement of the specific type shown in Figure 2, the interaction between them defines the quantum electrochemistry or the tunneling spin that can occur between them, namely:

The transition/tunneling $|0\rangle \leftrightarrow |h\rangle$ is associated with the so-called “nuclear mass defect”, and corresponds to the quantum-electrochemical potential given by the law of variation:

$$\Delta\Pi_B = \alpha_1 \exp(-\beta_1 \Delta H) \quad (6)$$

with the activation parameters and the reaction rate limiters to be determined for each kind of matrix adjacent beside the bondon formation enthalpy;

Similarly, the transition $|0\rangle \leftrightarrow |e\rangle$ correlates the quantum-electrochemical rate and potential with Gibbs bonding energy ΔG in this adjacency:

$$\Delta\Pi_\chi = \alpha_2 \exp(-\beta_2 \Delta G) \quad (7)$$

and corresponds to the specific activation (selection) of an isomeric topology from the set of topo-electron graphene isomers in the system;

Finally, the quantum tunneling of a defective hole – topological defect $|h\rangle \leftrightarrow |e\rangle$ corresponds to a “cellular” transition with the creation/annihilation topological potential:

$$\Delta\Pi_{EC50} = \alpha_3 \exp(-\beta_3\Delta A) \quad (8)$$

associated with the rate of creation/boson annihilation ΔA (in bondon, or inter-bosonic in bondots).

3.5 Graphene Quantum Electrochemistry. *Quantum-Electrochemical Metrology*

The previous phase is completed with experimental studies vs. the conceptual-computational estimates of the quantum tunneling current (in the quantum deca-nano-transistor $|0\rangle \times |e\rangle \times |h\rangle$ obtained by matrix multigraphene configurations), with the estimated intensity:

$$i(\varepsilon) = -\frac{2e}{\eta} \int_{\varepsilon}^{\infty} f(E_D) dE_D \quad (9)$$

for the clustering of quantum dots (bondons) in bondots (\mathcal{D}).

Here occurs the “comb” function of the Dirac multi-function specific for the bondots:

$$f(E_D) \equiv \sum_{q=-\infty}^{q=+\infty} \delta(q - E_D) \quad (10)$$

with the multi-energy tunneling effect of the Coulomb blockade specific to isolated (fullerene) electrons, respectively observable by the Raman specific displacements for different assemblies of the graphene oxide fullerene (Figure 6).

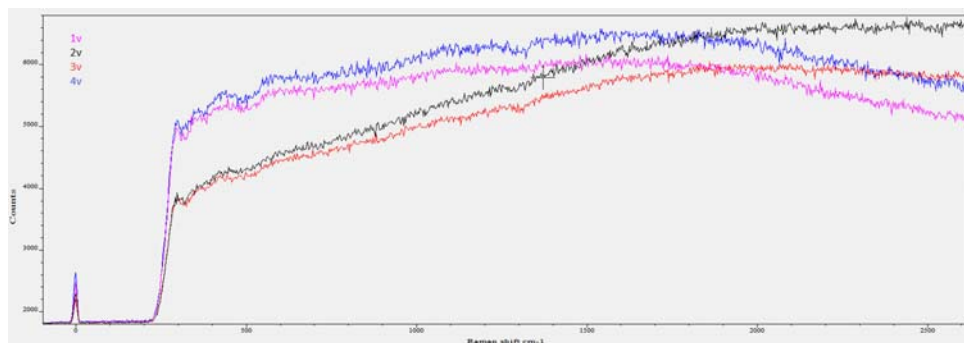


Figure 6. The Raman spectroscopy of quantum currents for bondots (bondon aggregates) formed in fullerenic graphenes (nominated as 1v, 2v, 3v, and 4v)

3.6 Photo-Activation of Spin Density on Graphene Semiconductor. *Activation of Quantum Logic Gates on Defective Graphene*

The deca-nano graphene transistor from the previous stage can be in the last phase “enriched” with quantum logic-gate properties by functionalization (on a graphene substrate) with molecular machines (motors) (Figure 7-left) in the 2nd stage. Furthermore, the acid-base

(deprotonation, reprotonation) of the molecular motor can be associated with distinct signal inputs in the conjugate system (graphene + molecular machines) with the specific signal (isolated or by photoactivation or spin coupling respectively in the quantum graphene transistor) of the analog type (direct current) or digital (“comb” current signal), see the last phase bondotic current, Figure 6, and Figure 7-right.

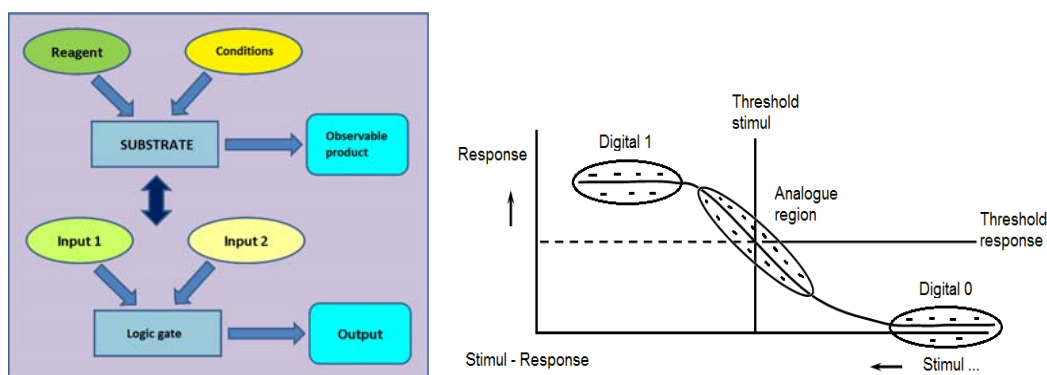
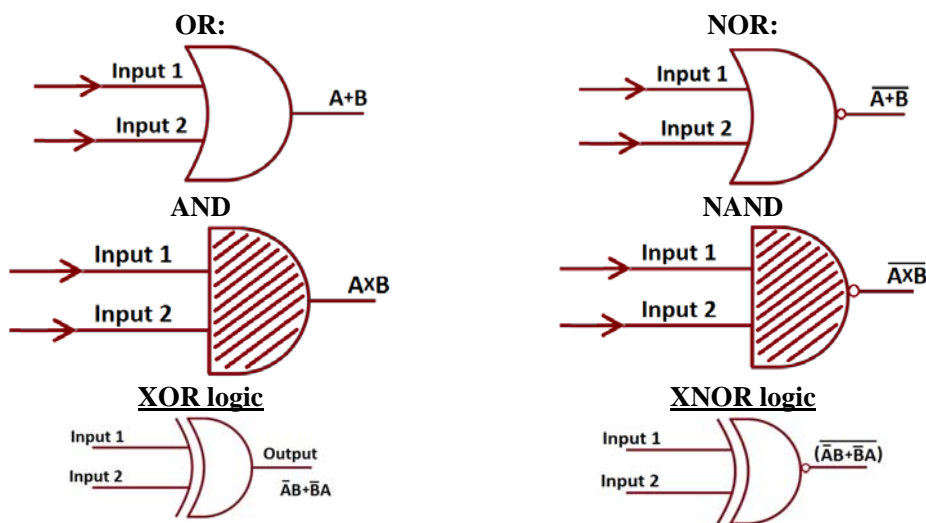


Figure 7. (a) Left - The conceptual design of a logic gate functionalization [24] (for example, molecular machines, protonation input processes, deprotonation, reprotonation, etc.) on a graphene substrate with an obvious response. (b) Right – conceptual design of the analog type (non-stationary, continuous), or of the digital type (stationary, quantum, Dirac “comb”)

These unique characteristics of the complex graphene system + the molecular machines make the bondots ideal candidates for further development for what is called molecular quantum algebra, in this case with graphene layers, in junctions and logical combinations that allow the obtaining of filtered, intelligent, controlled signals, and finally integrable into quantum moletronics, semiconductor, diode, quantum transistor and their applications.

It should be noted that logic gates are switches that have an output (0 or 1) that depends on the input (0 or 1). The list of logic gates, respectively digital switches for the molecular machine systems to be implemented and tested in this project is shown below in Figure 8.



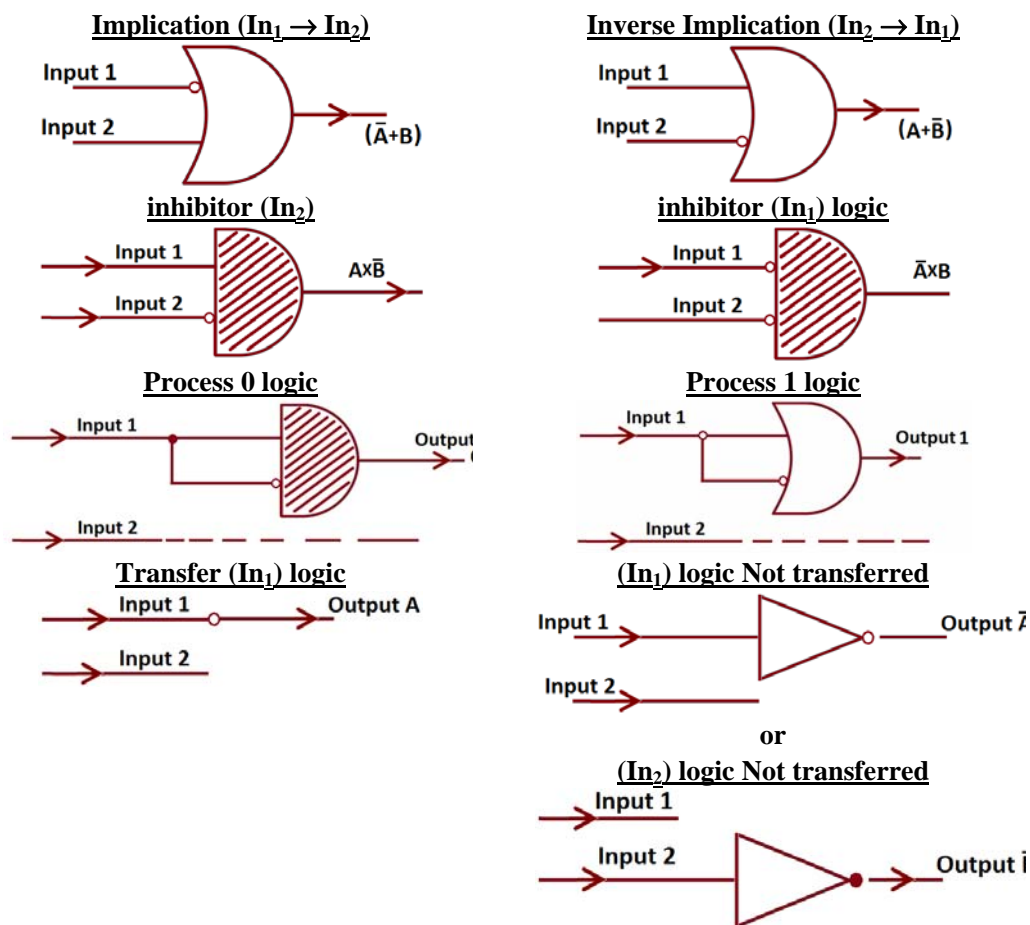


Figure 8. The list of logic gates, respectively digital switches for the molecular machine systems to be implemented and tested

The current estimations, based on the first atomic microscopy tests on graphene, non-functionalized with molecular machines, suggests the formation of stable over-micro-currents (by about 15%), thus analogous, as a result of increasing defects from the first photoactivation cycle, based on the collective aggregation of bondots, bondons, quantum couplings of electrons in the graphene conduction band. Thus, a digitalization effect of these analog signals (Figure 7-right) is expected in the case of the functionalization of these multi-graphene systems, matrix-deposited, with molecular motor machine-logic gates.

This way, Bose-Einstein's collective condensation can be controlled on the functionalized graphene with molecular machines, with the formation of super-micro-currents, integrable in moletronic circuits, and molecular algebraic calculus, with the establishment of quantum logic gates, conversion, but also intelligent storage and filtering, possibly activated by multi-graphene solar cells.

3.7. Photo-Activation of Spin Density on Graphene Semiconductor. *Supraconductivity of Deca-Nano-Magnetized Graphene Semiconductor*

The last phase, integrating the present research, extends the activation mode of the graphene system + molecular machines through the quantum spin coupling, along with the effect of magnetization, possibly induced by the specific form of adhesion in matrix multigraphene depositions (Figure 2). The specific quantum spin effect (magnetization) is shown in Figure 9 (combined detail of Figures 2 and 3, first phases of research) and the data of the material analysis in Table 1.

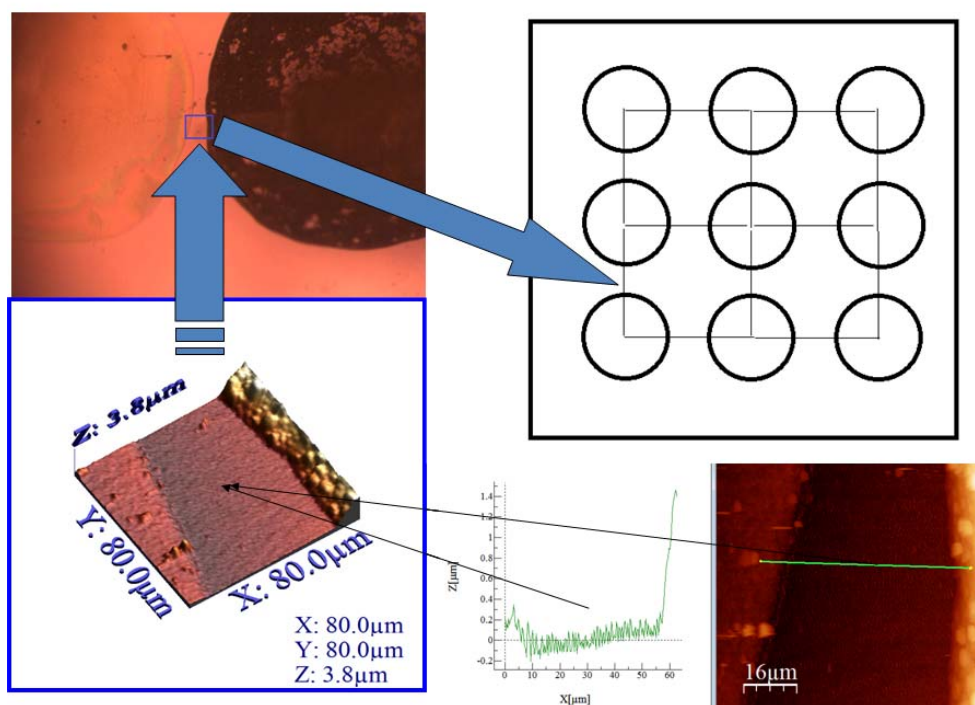


Figure 9. (a) Top-left - The microscope image at the closest distance between GO (left) and TiO_2 (right) as a detail of the matrix configuration in Figure 2. (b) Bottom-right - AFM and 3D analysis. (c) Bottom-middle - Material roughness on selected area (with global data in Table 1)

Table 1: The data obtained from the AFM image for the GO- TiO_2 adjacent configuration in Figure 2 and details from Figure 9

Sample name	Area [ironed surface] (μm^2)	Sa [roughness average] (nm)	Sq [RMS roughness] (μm)	Sp [maximum value] (μm)	Sv [minimum value] (μm)	Sy [peak to peak] (μm)	Sku [surface kurtosis]	Ssk [surface skewness]
1	6875.48	0.39	0.63	3.59	-0.23	3.82	9.49	2.69

The AFM technique observation was performed on the smallest distance between the GO and TiO_2 deposition to obtain a complete AFM image including both deposited and non-deposited area (ITO).

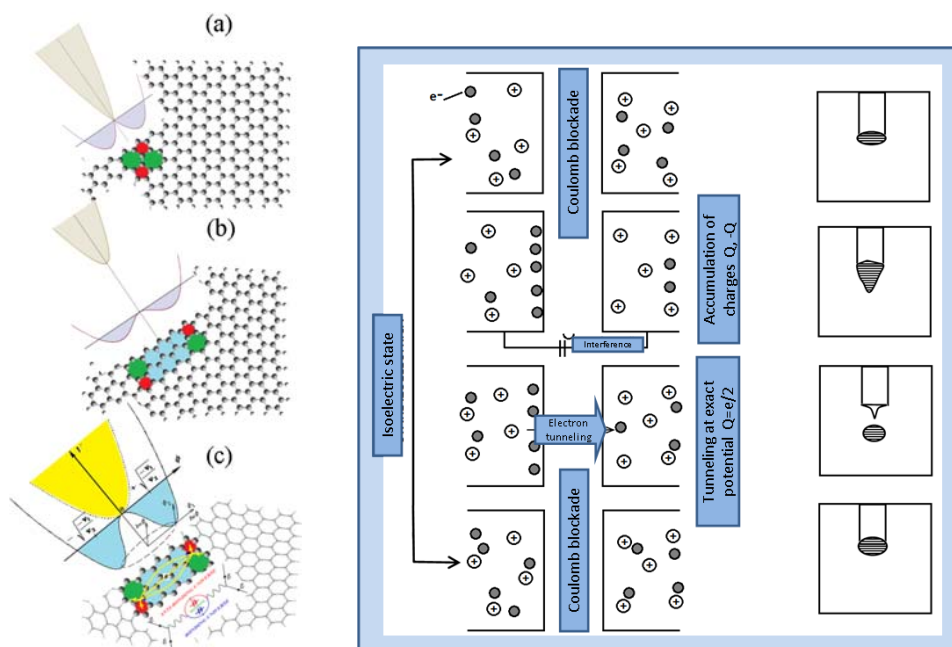


Figure 10. (a) Left - Tripartite vibrational instability on Graphene Network with Stone-Wales topological rotation vs. the breakage of symmetry in the spin coupling and the bosonization of the fermions, with the appearance of specific bondons: 1) the Jahn-Teller effect (through the canonical potential intersection), 2) the effect of the pseudo Jahn-Teller effect, 3) the Renner-Teller effect (see also the text for details).

(b) Right - schematic representation of the Coulomb blockade [24], in which the change in the electrostatic potential expresses the charge tunneling/redistribution. The Coulomb blockade allowed precise (metrological) control of the number of electrons and pairs of bondons and formed bondot trains (as a digital signal) in logic switches/gates (such as graphene complex system + molecular machines), allowing design advanced graphene integrated circuits (see graphenetrionic engineering)

The phenomenological basis of this type of internal activation (in addition to photo-activation) lies in the tunneling capacity and the type of adhesion in the multi-graphene matrix system (Figure 2). Thus, a gradual change of spin - electron spin coupling occurs in the bondonic boson, with the activation of magnetism (spin alignment or spin anti-alignment) on controlled areas of the multi-graphene matrix, depending on the type of potential coupling (double fermion vs. parabolic bosonic unit) described in Figure 10-left. Even more interesting, a correlation can be established between the three types of magnetic activation, the Jahn-Teller effect (symmetry breaking effect in the bosonization of the fermions, the first coupling of the quantum degenerated states), the pseudo-Jahn-Teller effect (the second order coupling of non-degenerate quantum states), and the Renner-Teller effect (the second order coupling of degenerate quantum states) with the three types of graphene states specifically to the quantum deca-nano-transistor, $|0\rangle \times |e\rangle \times |h\rangle$, studied in the 3rd stage. Furthermore, these three phases (quantum phase transitions, concerning the production of digital signals) correspond to the three phases of the Coulomb blockade (Figure 10-right), respectively surpassed, induced by magnetic activation and thus finally controlled.

4. CONCLUSIONS

The present research devoted to Graphenetrionics with Quantum Spin Electrochemistry develops disruptive applicative algorithms in photo-electro-chemistry with multiple possibilities for the development of efficient nano-energy solutions. Regarding the contribution of the recent studies in the field, the proposed research is provided with an innovative character, which is even more pronounced by the proposed magnetically activation (via the electrochemistry of the coupling by spinning) following an original multi-graphene matrix type deposition. Thereby, the matrix logic gates at the graphene neighborhood level areas supported by quantum induction (quantum electrochemistry) the activation of molecular machines as local quantum logic gates in the multi-graphene matrix nodes, thus achieving gate-in-gate systems with multi-potential electronic control, transfer in electronic pairs (bondons, bondots), digital signal communication and deca-control of nano-energy efficiency.

ACKNOWLEDGEMENT

We hereby acknowledge the research project PED123/2017 of UEFISCDI-Romania.

REFERENCES

1. Ferrari, A.C. et al. Science and technology roadmap for graphene, related two-dimensional crystals, and hybrid systems. *Nanoscale* **2005**, 7, 11, 4587-5062.
2. Cataldo, F.; Putz, M.V.; Ursini, O.; Angelini, G.; Garcia-Hernandez, D.A.; Machado, A. A new route to graphene starting from heavily ozonized fullerenes: Part 1: Thermal reduction under inert atmosphere. *Fuller. Nanotub Carb. N.* **2016a**, 24, 1, 52-61.
3. Cataldo, F.; Putz, M.V.; Ursini, O.; Angelini, G.; Garcia-Hernandez, D.A.; Machado, A. A new route to graphene starting from heavily ozonized fullerenes: Part 2: Oxidation in air. *Fuller. Nanotub Carb. N.* **2016b**, 24, 1, 62-66.
4. Cataldo, F.; Putz, M.V.; Ursini, O.; Angelini, G.; Garcia-Hernandez, D.A.; Machado, A. A new route to graphene starting from heavily ozonized fullerenes: Part 3: An electron SPIN resonance study. *Fuller. Nanotub Carb. N.* **2016c**, 24, 3, 195-201.
5. Putz, M.V.; Ori, O. Predicting bondons by Goldstone mechanism with chemical topological indices. *Int. J. Qua. Chem.* **2015**, 115, 3, 137-143.
6. Ludbrook, B.M.; Levy, G.; Nigge, P.; Zonno, M.; Schneider, M.; Dvorak, D.J.; Veenstra, C.N.; Zhdanovich, S.; Wong, D.; Dosanjh, P.; Straßer, C.; Stöhr, A.; Forti, S.; Ast, C.R.; Starke, U.; Damascelli, A. Evidence for superconductivity in Li-decorated monolayer graphene. *PNAS* **2015**, 112, 11795-11799.
7. Balzani, V.; Credi, A.; Venturi, M. Molecular devices and machines, *Nanotoday*, **2007**, 2, 18-25.
8. Balzani, V.; Credi, A.; Raymo, F.M.; Stoddart, J.F. Artificial molecular machines, *Angew. Chem. Int. Ed.*, **2000**, 39, 3348-3391.
9. Sauvage, J.P.; Dietrich-Buchecker, C. (Eds.), *Molecular Catenanes, Rotaxanes and Knots*, Wiley-VCH, Weinheim, **1999**.
10. Abendroth, J.M.; Bushuyev, O.S.; Weiss, P.S.; Barrett, C.J. Controlling motion at the nanoscale: rise of the molecular machines, *ACS Nano*, **2015**, 9, 7746-7768.

11. Venturi, M.; Credi, A. Electroactive [2]catenanes, *Electrochim. Acta*, **2014**, *140*, 467-475.
12. Ashton, P.R.; Ballardini, R.; Balzani, V.; Baxter, I.; Credi, A.; Fyfe, M.; Gandolfi, M.T.; Gomez-Lopez, M.; Martinez-Diaz, V.; Piersanti, A.; Spencer, N.; Stoddart, J.F.; Venturi, M.; White, A.J.P.; Williams, D.J. Acid-Base Controllable Molecular Shuttles, *J. Am. Chem. Soc.* **1998**, *120*, 11932-11942.
13. Garaude, S.; Silvi, S.; Venturi, M.; Credi, A.; Flood, A.H.; Stoddart, J.F. Shuttling Dynamics in an Acid-Base-Switchable [2]Rotaxane, *ChemPhysChem*, **2005**, *6*, 2145-2152.
14. Fyfe, M.C.T.; Glink, P.T.; Menzer, S.; Stoddart, J.F.; White, A.J.P.; Williams, D.J. Anion-assisted self-assembly, *Angew. Chem. Int. Ed. Engl.*, **1997**, *36*, 2068-2070.
15. Bissell, A.; Cordova, E.; Kaifer, A.E.; Stoddart, J.F. A chemically and electrochemically switchable molecular shuttle, *Nature*, **1994**, *369*, 133-137.
16. Arduini, A.; Bussolati, R.; Credi, A.; Pochini, A.; Secchi, A.; Silvi, S.; Venturi, M. Rotaxanes with a calix[6]arene wheel and axles of different length. Synthesis, characterization, and photophysical and electrochemical properties, *Tetrahedron*, **2008**, *64*, 8279-8286.
17. Balzani, V.; Credi, A.; Venturi, M. *Molecular Devices and Machines. Concepts and Perspectives for the Nanoworld*, Wiley-VCH, Weinheim, **2008a**.
18. Balzani, V.; Credi, A.; Venturi, M. Molecular machines working on surfaces and at interfaces, *Chem. Soc. Rev.*, **2008b**, *9*, 202-220.
19. Credi, A.; Balzani, V.; Langford, S.J.; Stoddart, J.F. Logic operations at the molecular level. An XOR gate based on a molecular machine, *Journal of the American Chemical Society* **1997**, *119*, 11, 2679-2681.
20. Putz, M.V.; Mirica, M.C. Eds. *Sustainable Nanosystems Development, Properties, and Applications*, IGI Global, Hershey Pasadena, USA, **2016**.
21. Venturi, M.; Iorga, M.I.; Putz, M.V., Molecular Devices and Machines: Hybrid Organic-Inorganic Structures, *Current Organic Chemistry* **2017**, *21*, 27, 2731-2759.
22. "The Nobel Prize in Chemistry 2016". *Nobelprize.org*. Nobel Media AB 2014. Web. 1 Nov **2016**. http://www.nobelprize.org/nobel_prizes/chemistry/laureates/2016/
23. Iorga, M.I.; Mirica, N.; Putz, M.V., Nano-electrochemistry. Part.II. Molecular machines, *Proceedings of the 23rd International Congress of Chemical and Process Engineering CHISA 2018*, 25-29 August **2018**, Prague, Czech Republic, P1.127, p.62.
24. Iorga, M.I.; Putz, M.V., Application of Molecular Machines in Photo-electrochemistry, In *Proceedings of The 24th International Symposium on Analytical and Environmental Problems*, University of Szeged, Hungary, 8-9 October 2018, Alapi T., Ilisz I., Eds., Published by University of Szeged, **2018**, pp.363-367.

Research Note

TOPOLOGICAL EVOLUTION OF THE 5|8|5 DEFECT IN GRAPHENE

Ottorino ORI (1) and Mihai V. PUTZ (2,3,*)

1. Actinium Chemical Research, Rome, Italy
2. Laboratory of Renewable Energies-Photovoltaics, R&D National Institute for Electrochemistry and Condensed Matter –INCEMC–Timisoara, Timisoara, Romania
3. Laboratory of Structural and Computational Physical-Chemistry for Nanosciences and QSAR, Biology-Chemistry Department, West University of Timisoara, Timisoara, Romania

ABSTRACT

The divacancy 5|8|5 planar defect in graphene show a typical evolution that has been theoretically simulated in this paper by using standard topological modelling techniques. The results point out the ability of the topological roundness in describing complex structures of the graphene plane with several types of polygons. Present considerations, by matching literature findings based on DTF studies, allow a better understanding on the relative stability of various defects in graphene and, in particular, the role played by long-range interactions in sp^2 systems.

Keywords: topological efficiency index, topological roundness, 5|8|5 defect, graphene.

1. INTRODUCTION

The mathematical properties of graphenic structures based on their symmetry and topology is an important topic in modern material science. Graphene has in fact attracted expanding technological interest for its unordinary electrical properties like, for example, outstanding ballistic transport properties and longest mean free path at room temperature, distinctive integral and half-integral quantum hall effect and much more [1,2,3]. Graphene - *the miracle material* - has been considered since its discovery made in 2004 by the two Russian-born scientists, Andre Geim and Konstantin Novoselov, both Nobel laureate in 2010, as the ideal candidate material for the next *post-silicon electronics*. Its honeycomb (finite) lattice presents two different types of edges: armchair and zigzag, which largely influence the electronic properties of graphene [4,5]. The main limitation to the applications it is

represented by the *absence of a semiconducting gap in pristine graphene*. The search for industrial methods to create tunable band-gap in graphene poses significant challenges for graphene-based devices, since the introduction of defects showed potential solutions to this important aspect. On one side in fact electronic and mechanical properties of graphene get deteriorated by the presence of structural and topological defects appearing during the lattice growth. On the other side however, deviations from atomic periodicity make it possible to achieve new functionalities. Defects can be introduced into graphene, for example, by irradiation or chemical treatments. The flatness of the graphene sheet mainly descends from the sp^2 -hybridized states of the carbon atoms composing the layer. This chemical characteristic allows a cascade of interesting rearrangements of the carbon atoms that may form various type of polygons tiling the graphenic layer, breaking in such a way the perfect hexagonal symmetry of the pristine flat lattice. Many different structures may be created with the usage of non-hexagonal rings, influencing in such a way the local curvature depending from the type of defective (non-hexagonal) polygons that are present. For example, an isolated pentagon induces the formation of a nano-cone but on the contrary, two pentagons connected by an octagon (5|8|5defect) leave the lattice locally flat [6,7]. This huge variety of morphological properties is not offered by bulk crystals like diamond or semiconductors that are made by sp^3 atoms. Very important to notice that the “reconstructions in the atomic network permit a coherent (topologically) defective lattice without under coordinated atoms” [8] allowing the generation of two classes of defects in the sp^2 mesh. We have in fact i) point defects (vacancies or interstitial atoms) that are zero-dimensional and ii) 1D linear defects, each defect showing a certain mobility, exponentially increasing with the temperature, in the graphene plane with defect-specific activation barriers.

In this note, we focus on the *topological evolution* of the 5|8|5defect that has important influences on chemical, electronic, magnetic, and mechanical properties of graphene-based nanodevices. We shall not consider here the mechanisms that lead to the formation of this type of defect because the authors already have devoted a specific work [7] to the topic, proposing an original and fully isomeric mechanism based on the usage of *smart sequences* of Stone-Wales (SW) rearrangements of the pristine hexagonal plane. This isomeric model provides a valid alternative to the 2-vacancy mechanism that is normally invoked in literature [8] to describe the origin of the 5|8|5defective region with an energy barrier of about 8eV, say 4eV per vacant atom. Topological reorganizations of large portion of the graphene lattice have a lower probability of formation (having the standard 5|7|7|5 SW defect a formation energy of about 10eV [9] these rotations present in fact high activation barriers), nevertheless these kinds of mechanisms are important not only from the theoretical point of view, allowing a much profound understanding about the behaviors of the sp^2 networks in presence of non-hexagonal polygons, but also from practical reasons since ion irradiation or rapid temperature quenching create the conditions that lead to the formation of SW-type rearrangements in fullerenes or graphenic planes, these unfavored routes may play a role in the creation of defects in graphene plane or graphenic regions (i.e. made by hexagons) in large fullerenes [9,10,11].

2. TOPOLOGICAL INVARIANTS

Consider G being a chemical graph with N nodes and B bonds. Distance-based topological invariants have been extensively applied to simulate stability/reactivity of hexagonal systems seen as graphs [12], in which the *chemical distance* d_{vu} is merely the

number of bonds connecting, along the shortest path, the two nodes v and u , with $d_{vv}=0$ by definition. With the name Wiener-weight w_v of the node v we call the invariant:

$$w_v = \frac{1}{2} \sum_{u=1}^N d_{vu} \quad (1)$$

According with the topological modeling approach, graph invariant (1) represents a powerful atomic descriptor having peculiar prerogatives: a) w_v it is inversely proportional to the *reactivity* of the node b) and inversely proportional to the *compactness* of the graph. The Wiener index W of the whole graph is just the sum of the Wiener-weights:

$$W = \sum_{v=1}^N w_v \quad (2)$$

Moreover, w_v allows c) the direct *topological measure* of the *topological roundness* of the graph, expressed in this case by the *extreme topological efficiency index* ρ^E :

$$\rho^E = \frac{\underline{w}}{\overline{w}}; \quad \rho^E \geq 1 \quad (3)$$

in which $\underline{w} = \min\{w_v\}$ and $\overline{w} = \max\{w_v\}$. The most *compactly-embedded* vertices of G (the so-called *minimal vertices* or *minimal nodes*) have Wiener-weight equal to \underline{w} . Invariant (3) awards the ability of graph nodes to be connected to the other vertices with an efficiency comparable to the one of the minimal vertices; highly efficient graphs like graphene periodic lattice tend therefore to minimize ρ^E , i.e. to have $\rho^E \sim 1$. Topological roundness is considered here to act like a topological potential $\Phi^E = \rho^E$ driving the systems toward the “most round” topological configurations by minimizing the ρ^E value. It is worth noticing here that the topological descriptors given by Equations (1-3) are built on the chemical distances d_{vu} connecting *any pairs* of atoms in the system. These descriptors, and in particular the topological potential Φ^E are in this way able to naturally describe the effects of long-range interactions in sp² graphene lattices.

This fast and elegant computational model is applied once more in this article to describe the evolution of a defective graphenic lattice with a 5|8|5 defect. The lattice reconstruction process leads to complex modifications of “the electronic charge density and this varies the bond lengths within and around” the 5|8|5 defect [13] preserving the *local flatness* of the defective lattice. This pentagon-octagon-pentagon linear structure, like the one embedded in the 6x4 hexagonal super-cell G_0 represented in Figure 1, maintains the sp² hybridization state. The graphene-flake G_0 consists in 96 nodes and B=144 bonds if periodic boundary conditions are imposed in both directions (Figure 1a). All the atoms are topologically equivalent $\rho^E(G_0) = 1$ with $\underline{w}(G_0) = \overline{w}(G_0) = 260$ and $W(G_0) = 24960$.

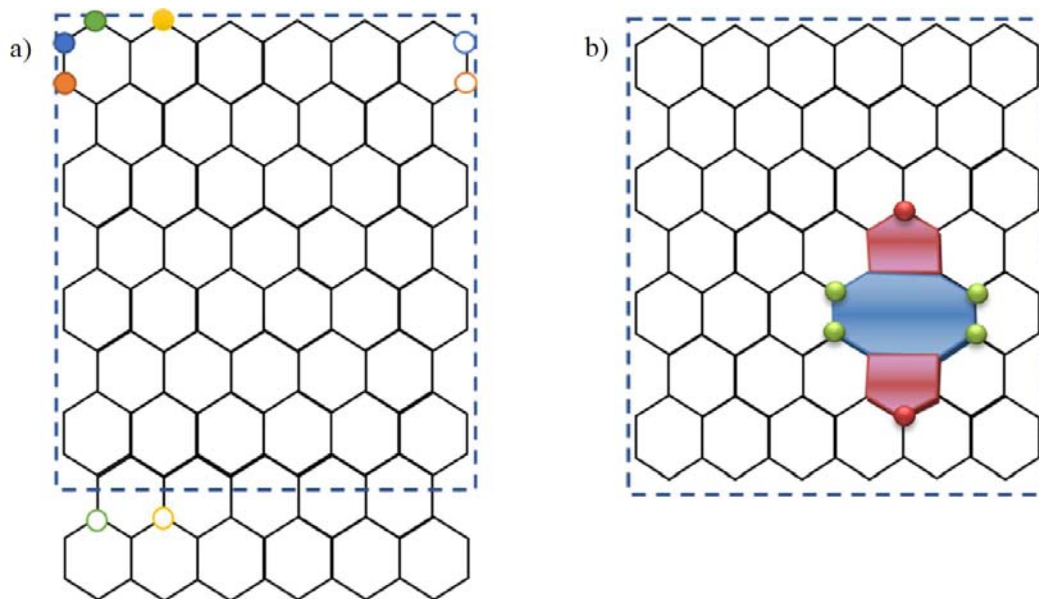


Figure 1.a) The original G_0 6x4 super-cell (dashed rectangle) has 96 atoms with 3 bonds each when the periodic conditions are applied in both directions (solid and circled balls with the same colors are connected by 1 periodic bond). b) The polygons forming the 5|8|5 defect are 2 pentagons (red) and 1 octagon (blue), the remaining hexagons are in white; this periodic super cell G_{585} has 94 nodes still with 3 bonds each.

The polygons forming the 5|8|5 defect are pictured (Figure 1b) in red (pentagons) and blue (octagon) and they are embedded in the hexagons (white) of the pristine graphenic lattice. The defective graphenic system G_{585} shows now 94 nodes (the 5|8|5 defect is generated by a divacancy so G_{585} has two atoms less than G_0) and $B=3N/2=141$ bonds still under periodic boundary conditions. The presence of the non-hexagonal rings breaks in G_{585} the symmetry of the nodes. Now the minimal nodes are the 4 nodes placed pairwise on the opposite sides of the octagon represented with green balls in Figure 1b. These minimal vertices have $\underline{w}(G_{585})=244.5$ and they represent, in the topological picture, the most stable atoms of the systems. On the other hand, the 2 red balls with $\overline{w}=256.5$ that sit on the pentagons, indicate the two most reactive nodes of G_{585} . The topological roundness passes in this way to the $\rho^E(G_{585}) = 1.04907975$ and the Wiener index is $W(G_{585}) = 23619$. The topological efficiency is increased by the presence of the 5|8|5 defect and the fact that $\rho^E(G_{585}) > \rho^E(G_0)$ evidences the energy cost that is necessary to create the divacancy structure. This barrier has been determined to be 8eV, approximately “of the same order of the single vacancy formation” with the evident gain, since two atoms are missing, in the energy permitting atom (4 eV per atom)” [9]. In literature several molecular simulation studies report in fact that two initially isolated vacancies in the graphene layer may coalesce into the 5|8|5 configuration that is the starting point G_{585} of the present research (Figure 1b). The 5|8|5 defect may in fact evolve toward other configurations of the graphenic lattice able to accommodate two missing atoms [9]. These configurations are generated via SW bond rotations and give rise to extended defects that are frequently observed in electron microscopy experiments [17] (see also references articles reported in [9]). The following section is

devoted to study the transformations of the 5|8|5 defect into the two standard configurations one may build via two successive SW flips: the triple pentagon-triple heptagon (555-777) defect and then the quadruple pentagon / hexagon / quadruple heptagon(5555-6-7777) most stable defect [13]. Our computation will be based on the variations of the topological indices induced by the SW rotations on the periodic super-cell made of 94 sp^2 atoms whose starting configurations is represented by $G_{555-777}$ (see Figure 1 and Figure 2 below).

3. TOPOLOGICAL SIMULATION AND DISCUSSIONS

The first rearrangement of the $G_{555-777}$ lattice that allows an energy gain of about 0.9 eV [14,15,16] is obtained when one of the 2 side edges of the octagon is rotated with a typical SW rearrangement. In [14] authors also provide a direct evaluation of the energy gap of 0.8 eV still favoring the SW rotation. Recent DFT computations on the same configurations still favor the rotation of the edge of the octagon evidenced in Figure 2a with the arrow, but they reduce the energy gain to 0.53 eV [13].

This SW rotation transforms the 5|8|5 defect into anew arrangement, energetically favored, made of three pentagons and three heptagons (the (555-777) defect) which is normally observed by the experiment study [17].The same defects may be formed on the surface of the carbon nanotubes (CNT's) with an energy gain that depends from the size and from the chirality of the system [14]. Large armchair (zigzag) nanotubes, with diameter of about 40 Å (53 Å), behave like graphene (and this is quite logic due to the low curvature of the cylinders). For small nanotubes however the 5|8|5 defect is instead *most stable* than the (555-777)one and the zigzag chirality plays again against the (555-777) defect when CNT's with small diameter are considered. Analogous results are reported for graphene finite sized portions (graphene flakes) in the recent article [16].

The $G_{555-777}$ lattice presents, after the first SW, the (555-777) morphology given in Figure 2b. The octagon has disappeared replaced by a more complex structure with a three-fold configuration that includes three fused heptagons plus three satellite pentagons. The graph $G_{555-777}$ is characterized by the new invariants $\rho^E(G_{555-777}) = 1.06498952$ and $W(G_{555-777}) = 23514$. In this case then the topological potential E^E plays against the SW rotation that causes the passage from $G_{555-777}$ to lattice $G_{5555-6-7777}$. Both defects are present in graphene layers and reversible $G_{555-777} \leftrightarrow G_{5555-6-7777}$ switching is also reported [9].

A second SW rotation may take place acting on the bond shared by one of the heptagons and the external hexagon, indicated with the arrow in Figure 2b;in this way the lattice assumes a novel “quadrupolar” structure named (5555-6-7777) defect. In literature, the formation energy of this quadrupolar defect has been found between those of 5|8|5and (555-777) [9] whereas other DFT calculations consider [13]the difference in the formation energy between the two defective configurations (5555-6-7777)and (555-777)quite small of the order of ~ 0.1 eV. Figure 2c represents the periodic super-cell of the $G_{5555-6-7777}$ graph having topological roundness of $\rho^E(G_{5555-6-7777}) = 1.02801856$ and $W(G_{5555-6-7777}) = 23482$.

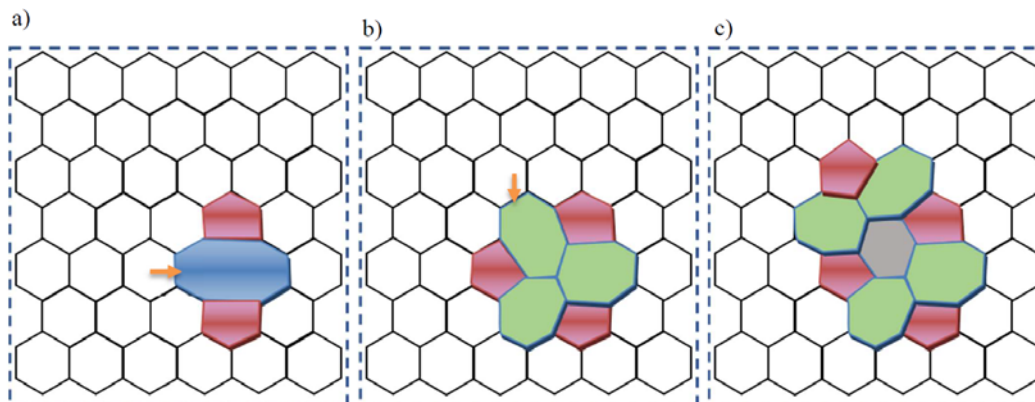


Figure 2. a) The G_{585} lattice; the arrowed bond allows a SW rotation that produces defect (555-777) represented in b). By rotating the bond indicated with the arrow in b) the (5555-6-7777) quadrupolar configuration is produced c). Rings colored in red, green, blue, rings have 5,7,8 carbon atoms respectively. Hexagons are colored in white and gray.

Figure 3 summarizes the behaviors of the topological potential $\Xi^E - \rho^E$ in the various passages that transform the pristine graphene lattice G_0 in the final divacancy graphene with the quadrupolar structure $G_{5555-6-7777}$.

The first part of the curve shows the response of the topological potential to the creation of a single vacancy SV and then to the introduction of the second vacancy DV that allows the generation of the 5|8|5 rearrangement in the graphene lattice. The creation of the single vacancy SV breaks the perfect symmetry of the periodic graphene super-cell G_0 by creating a three-fold “crater” in the honeycomb mesh increasing the value of the topological potential Ξ^E . The introduction of the second vacancy is obtained by eliminating one of the 3 atoms that SV leaves with one dangling bond, with the creation of a symmetric DV hole with two mirror planes. The topological potential Ξ^E (DV) does not therefore vary too much in respect to Ξ^E (SV) confirming the results obtained by ab-initio simulations [9] that indicate that the formation energy of DV is close to the SV one, about 8 eV. The topological model predicts the evolution of the DV lattice toward the 5|8|5 configuration whose increased stability is signaled by the Ξ^E reduction (see Figure 3). The topological model fails, when compared with the results of ab-initio simulations (see previous section) in predicting the passage from the G_{585} lattice to the defective graph (555-777) represented in Figure 1a, 1b. The topological efficiency is larger for the (555-777) and from the topological point of view the systems therefore privileges the 5|8|5 configuration. Finally, the quadrupolar structure $G_{5555-6-7777}$ presents a topological stability in terms of Ξ^E that is comparable with the one of the G_{585} lattice. This last result confirms the study [9] in which the authors state that the formation energy of the (5555-6-7777) defective lattice “is between those of 5|8|5 and (555-777)”.

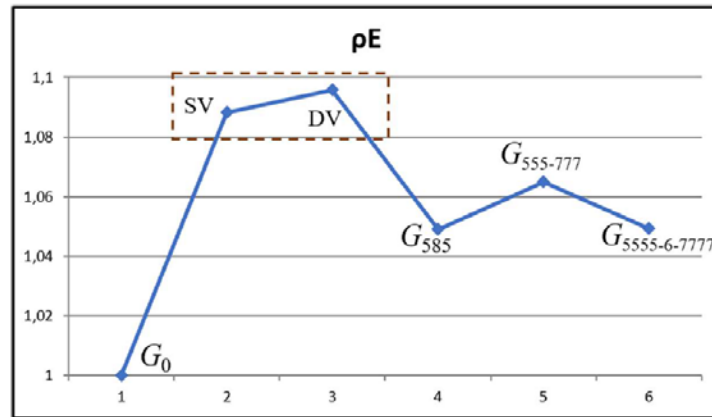


Figure 3. The curve of the topological roundness ρ^E is given for the various defective lattices that are created starting from the pristine graphene super cell G_0 with the introduction of a single vacancy SV and a double vacancy DV.

Figure 3 shows that, ranked by ρ^E , the 3 competing lattices with a DV show the stability sequence 5|8|5, (5555-6-7777) and (555-777). This result is compatible with the TEM observed transitions [18] among defective configurations $G_{585} \leftrightarrow G_{555-777} \leftrightarrow G_{5555-6-7777}$.

Once more, our study points out the *somehow surprising* ability of the topological roundness to simulate, in a negligible amount of CPU time, the physical behavior of complex sp^2 carbon systems. The method gets boosted by the natural (and computationally easy way) the topological invariants have for taking into consideration long-range interactions between all pairs of atoms in large nanostructures.

4. CONCLUSIONS

The simulations of defective graphenic lattices based on topological potentials like the topological roundness produce interesting answers concerning relative stability lattices with a divacancy, predicting an apparent predominance of the pentagon-octagon-pentagon defect, followed by the quadrupolar DV rearrangement.

Therefore, further insight by determination of energetic and thermodynamic quantities with observable character are needed, including the combination of the present topological approach with the “bondon” quasi-particle picture, an innovative physical entity corresponding to the quantum particle of the chemical bond [17], recently applied to investigate influence of topological long-range interaction on the properties of one-dimensional graphenic nanoribbons [18]. In such a picture the stability of a defective structure will be judged in terms of bondonic life-time for “covering” the super-cell of the system that is associate to the characteristic bondonic frequency; it also provides the route for the spectroscopic detection of the bondonic states through Raman, Compton or allied solid state techniques.

Our results shed new light on the fundamental processes that dominate the rearrangement of carbon networks, and the processes that we investigate in this study are likely be replicated in the formation of other carbon nanostructures from carbon vapor, such as nanotubes and fullerenes. Moreover, present topological investigations are worth to be extended to non sp^2

systems like the black phosphorus that is currently targeted by many experimental investigations and detailed ab-initio theoretical studies [19] dealing with the role of SW rotation and SV and DV in creating defects in black phosphorus motivating further topological investigations in the area of material with tunable band-gaps and magnetic fictionalization.

REFERENCES

- [1] Geim, A.K., 2009. Graphene: status and prospects. *science*, 324(5934), pp.1530-1534.
- [2] Jariwala, D., Sangwan, V.K., Lauhon, L.J., Marks, T.J. and Hersam, M.C., 2013. Carbon nanomaterials for electronics, optoelectronics, photovoltaics, and sensing. *Chemical Society Reviews*, 42(7), pp.2824-2860.
- [3] Zhang, Y., Tan, Y.W., Stormer, H.L. and Kim, P., 2005. Experimental observation of the quantum Hall effect and Berry's phase in graphene. *Nature*, 438(7065), p.201-204.
- [4] Putz, M.V. and Ori, O., 2014. Bondonic effects in group-IV honeycomb nanoribbons with Stone-Wales topological defects. *Molecules*, 19(4), pp.4157-4188.
- [5] Koorepazan-Moftakhar, F., O. Ori O. & Ashrafi, A.R. (2018) Symmetry – Based Invariants of Nanostructures and Their Effect on Edge States of Carbon Nanotubes, Fullerenes, Nanotubes and Carbon Nanostructures, DOI: 10.1080/1536383X.2018.1558402
- [6] Bultheel, A. and Ori, O., 2018. Topological modeling of 1-Pentagon carbon nanocones—topological efficiency and magic sizes. *Fullerenes, Nanotubes and Carbon Nanostructures*, 26(5), pp.291-302.
- [7] Ori, O. & Putz, M. V. (2014) Isomeric Formation of 5|8|5 Defects in Graphenic Systems, *Fullerenes, Nanotubes and Carbon Nanostructures*, 22:10, 887-900,
- [8] L. Liu et al. "Defects in Graphene: Generation, Healing, and Their Effects on the Properties of Graphene: A Review" *Journal of Materials Science & Technology* 31 (2015) 599-606
- [9] Banhart, F., Kotakoski, J. and Krasheninnikov, A.V., 2010. Structural defects in graphene. *ACS nano*, 5(1), pp.26-41.
- [10] Dunk, P.W., Kaiser, N.K., Hendrickson, C.L., Quinn, J.P., Ewels, C.P., Nakanishi, Y., Sasaki, Y., Shinohara, H., Marshall, A.G. and Kroto, H.W., 2012. Closed network growth of fullerenes. *Nature communications*, 3, p.855.
- [11] Putz, M.V. and Ori, O., 2012. Bondonic characterization of extended nanosystems: Application to graphene's nanoribbons. *Chemical Physics Letters*, 548, pp.95-100.
- [12] Iranmanesh, A., Ashrafi, A.R., Graovac, A., Cataldo, F., and Ori, O. (2012) Wiener index role in topological modeling of hexagonal systems - from fullerenes to grapheme. In

Distance in Molecular Graphs – Applications; Gutman, I and Furtula, B. (eds.), Univ. Kragujevac: Kragujevac, pp. 135–155.

[13] Chen, Q., Robertson, A.W., He, K., Gong, C., Yoon, E., Lee, G.D. and Warner, J.H., 2015. Atomic Level Distributed Strain within Graphene Divacancies from Bond Rotations. *ACS nano*, 9(8), pp.8599-8608.

[14] Amorim, R.G., Fazzio, A., Antonelli, A., Novaes, F.D. and da Silva, A.J., 2007. Divacancies in graphene and carbon nanotubes. *Nano Letters*, 7(8), pp.2459-2462.

[15] Lherbier, A., Dubois, S.M.M., Declerck, X., Roche, S., Niquet, Y.M. and Charlier, J.C., 2011. Two-dimensional graphene with structural defects: elastic mean free path, minimum conductivity, and Anderson transition. *Physical review letters*, 106(4), p.046803.

[16] Liu, L. and Chen, S., 2017. Geometries and Electronic States of Divacancy Defect in Finite-Size Hexagonal Graphene Flakes. *Journal of Chemistry*, 2017.

[17] Girit, Ç.Ö., Meyer, J.C., Erni, R., Rossell, M.D., Kisielowski, C., Yang, L., Park, C.H., Crommie, M.F., Cohen, M.L., Louie, S.G. and Zettl, A., 2009. Graphene at the edge: stability and dynamics. *science*, 323(5922), pp.1705-1708.

[18] Kotakoski, J.; Krasheninnikov, A. V.; Kaiser, U.; Meyer, J. C. From Point Defects in Graphene to Two-Dimensional Amorphous Carbon. *Phys. Rev. Lett.* 2011, 106, 105505.

[19] Gaberle, J. and Shluger, A.L., 2018. Structure and properties of intrinsic and extrinsic defects in black phosphorus. *Nanoscale*, 10(41), pp.19536-19546.